

# Decontamination of Radionuclides from Concrete by Microwave Heating. I: Theory

Zdeněk P. Bažant, F.ASCE,<sup>1</sup> and Goangseup Zi<sup>2</sup>

**Abstract:** The paper analyzes a proposed scheme of decontamination of radionuclides from concrete structures, in which rapid microwave heating is used to spall off a thin contaminated surface layer. The analysis is split in two parts: (1) the hygrothermal part of the problem, which consists in calculating the evolution of the temperature and pore pressure fields, and (2) the fracturing part, which consists in predicting the stresses, deformations and fracturing. The former is assumed to be independent of the latter, but the latter is coupled to the former. The heat and moisture transfer governing the temperature and pore pressure fields induced by the decontamination process is analyzed using an improved form of Bažant and Thonguthai's model for heat and moisture transfer in concrete at high temperatures. The rate of the distributed source of heat due to the interaction of microwaves with the water contained in concrete is calculated on the basis of the standing wave normally incident to the concrete wall. Since the microwave time period is much shorter than the time a heating front takes to propagate over the length of microwave, and since concrete is heterogeneous, the ohmic power dissipation rate is averaged over both the time period and the wavelength. The reinforcing bars parallel to the surface are treated as a smeared steel layer. The recently developed microplane model M4 serves as the constitutive model for nonlinear deformation and distributed fracturing of concrete. Application of the present model in numerical computations is relegated to a companion paper which follows.

**DOI:** 10.1061/(ASCE)0733-9399(2003)129:7(777)

**CE Database subject headings:** Concrete; Microwaves; Contamination; Contaminants; Heating; Diffusion; Thermal stresses; Pore pressure.

## Introduction

Concrete is ubiquitous in nuclear facilities. As a consequence of their longtime operation, various radionuclides, such as strontium, cesium, cobalt, uranium, etc. (Spalding 2000), have gradually diffused from the environment into a surface layer of concrete. Although the radionuclide concentrations are very small, the exposure to radiation over many years could be hazardous to human health. Typically, the contaminated layer is only 1–10 mm thick [Fig. 1(a)] (White et al. 1995), and so a demolition of the whole structures is unnecessary. Nevertheless, to guarantee a safe long-time work environment, the contaminated layer needs to be removed and properly disposed of as nuclear waste.

Possible decontamination techniques include removal of the contaminated layer by hammer and chisel, by high-pressure water jet, and by various thermal treatments. This paper deals with the last, which can be of two types: (1) heat conduction from a heated surface, and (2) heating generated by microwaves throughout the volume of concrete. The former type has been studied for a long time with regard to fire resistance of buildings, and even more

deeply with regard to the effects of hypothetical nuclear reactor accidents (e.g., Bažant and Thonguthai 1978, 1979; Ahmed and Hurst 1997; Gawin et al. 1999). As a result, the material characteristics needed to calculate the temperatures and pore pressures due to heat conduction from a heated surface are known relatively well (Harmathy 1970; Harmathy and Allen 1973; Bažant and Kaplan 1996; Neville 1997; Vodák et al. 1997).

The recent studies of the decontamination process have emphasized microwave heating, which allows a much faster removal of the contaminated layer (within only about 10 s; White et al. 1995). The driving force of the spalling is the microwave heat source which is distributed through the volume of concrete and is generated by microwaves emitted from a powerful applicator [Fig. 1(a)].

Microwave heating has already been applied in various civil engineering problems. For instance, (1) microwaves have been extensively used for nondestructive evaluation of materials. (2) Microwave ovens (instead of the traditional ovens) have been used for effective drying of porous geomaterials (Wei et al. 1985). (3) Microwave heating has been used to accelerate the curing process of concrete at early ages (Watson 1968a; Moukwa et al. 1991). (4) Microwaves of low frequency and low power density were shown capable of heating properly insulated concrete specimens to an almost uniform temperature (Hertz 1981, 1983), which made it possible to measure the effect of temperature on compression strength in the absence of temperature gradients. (5) Microwaves of high frequency, which are suitable for the present decontamination process, have been shown capable of generating a localized field of high stress that can serve as a demolition tool (Watson 1968b; Wace et al. 1989; White et al. 1995).

Some valuable investigations of the microwave decontamination of concrete have already been undertaken. Li et al. (1993)

<sup>1</sup>McCormick School Professor and W. P. Murphy Professor of Civil Engineering and Materials Science, Northwestern Univ., 2145 Sheridan Rd., Evanston, IL 60208. E-mail: z-bazant@northwestern.edu

<sup>2</sup>Research Associate, Dept. of Civil Engineering, Northwestern Univ., 2145 Sheridan Rd., Evanston, IL 60208. E-mail: g-zi@northwestern.edu

Note. Associate Editor: Franz-Josef Ulm. Discussion open until December 1, 2003. Separate discussions must be submitted for individual papers. To extend the closing date by one month, a written request must be filed with the ASCE Managing Editor. The manuscript for this paper was submitted for review and possible publication on March 12, 2002; approved on October 29, 2002. This paper is part of the *Journal of Engineering Mechanics*, Vol. 129, No. 7, July 1, 2003. ©ASCE, ISSN 0733-9399/2003/7-777-784/\$18.00.

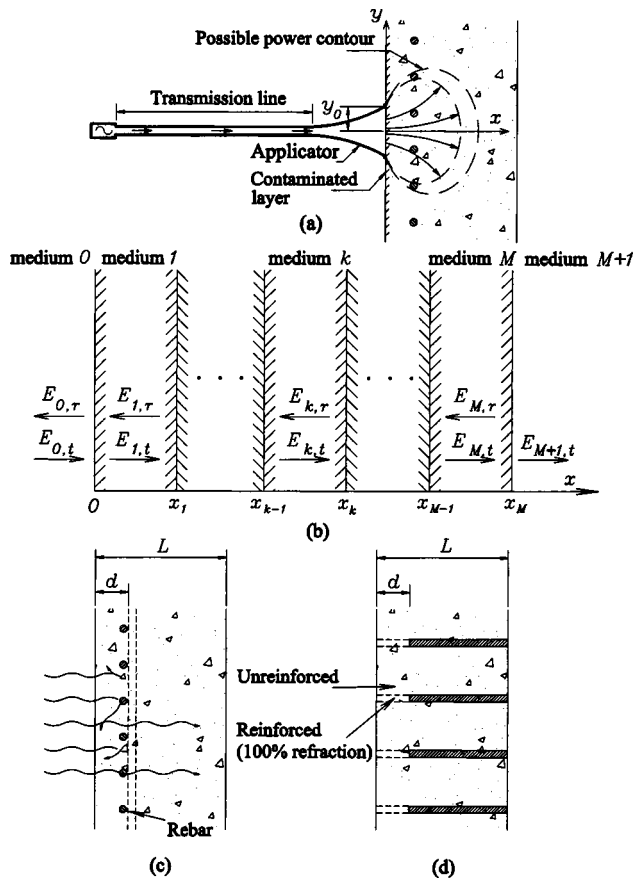


**Fig. 1.** (a) Sketch of microwave power decontamination system; (b) transmission (*t*) and reflection (*r*) of transmission electron microscopy wave at interfaces of different media; (c) typical layout of concrete wall and wave reflection by reinforcing bars and aggregates; and (d) partition of concrete body into reinforced segments and unreinforced segments

analyzed one-dimensional temperature profiles using a linear heat transfer model. Lagos et al. (1995) extended the heat transfer model to two dimensions and calculated the heat generation rate based on the standing wave normally incident to a homogeneous concrete wall. They smeared the reinforcing bars into an infinitely thin layer whose reflection factor was determined according to the area-ratio of the bars. They assumed the dielectric properties of concrete to be constant over the thickness of concrete during the decontamination process. However, they could not study the development of pore pressures because they did not model the moisture transfer coupled to the heat transfer. They assumed the surface layer to spall off when the compressive stress in the direction parallel to surface under a perfect restraint in that direction exhausts the compressive strength of the concrete. They did not take into account the deformation of the body surrounding the heated zone.

The practical objective of this study, which was summarized at a recent conference (Bažant and Zi 2001), is twofold: (1) to present a model-based mathematical analysis of microwave heating and spalling of concrete; and (2) to apply it to the decontamination process that takes into account not only the thermal deformation and surface layer restraint but also the moisture transfer, pore pressures, and overall deformation of the structure. The theory will be explained in this paper, while the companion paper that follows (Zi and Bažant 2003) will present the numerical ap-

plication. The constitutive, fracture, thermal, and diffusion models of concrete applied here are of course known. Nevertheless, since these models exist in different variants, and since some minor modifications were made in them in this project, they are briefly described in the Appendices of parts I and II of this study.

## Heat Generation by Transverse Electromagnetic Waves

The microwaves represent electromagnetic waves of frequency 300 MHz–30 GHz. The energy carried by electromagnetic waves through surface *S* is

$$-\int_S \mathcal{P} \cdot d\mathbf{S} = -\int_S \mathbf{E} \times \mathbf{H} \cdot d\mathbf{S} = \frac{\partial}{\partial t} \int_V (w_e + w_m) dV + \int_V p_\sigma dV. \quad (1)$$

(e.g., Cheng 1983) where  $\mathcal{P}$ =Poynting vector characterizing the power density of the electromagnetic wave,  $\mathbf{E}$ =electric field strength vector;  $\mathbf{H}$ =magnetic field strength vector;  $d\mathbf{S}=\mathbf{n}dS$ , where  $d\mathbf{S}$ =surface element and  $\mathbf{n}$ =its unit normal;  $V$ =volume of body;  $\epsilon=\epsilon'-i\epsilon''$ =complex dielectric permittivity;  $\mu=\mu'-i\mu''$ =complex magnetic permittivity;  $\sigma=\omega\epsilon''$ =dielectric conductivity;  $\omega=2\pi f$ =angular velocity;  $f$ =frequency,  $w_e=\epsilon E^2/2$ =electric energy density;  $w_m=\mu H^2/2$ =magnetic energy density;  $p_\sigma=\sigma E^2$ =ohmic power dissipation;  $t$ =time; and  $V$ =volume.

Because the heat generation rate is a function of the electric field strength, one needs to solve the electric field strength vector  $\mathbf{E}$  to obtain the heat source. On exit from the microwave applicator, the waves are guided and simple. But farther away the electromagnetic field can become complicated [Fig. 1(a)]. An accurate solution would have to be obtained numerically from the Maxwell equations, which is not a simple affair. For our purpose, however, an approximate solution can be obtained by using the solution of a standing electromagnetic wave, particularly the solution of a transverse electromagnetic wave normally incident to a half space of a dielectric material, the concrete. The heat source calculated in this manner needs of course some further adjustment to obtain the proper power distribution (Thuéry 1992).

## Electric Strength of Standing Electromagnetic Waves

Let us now review the solution of the transverse electromagnetic waves, which form a standing wave pattern. The propagation of electromagnetic waves is governed by the Maxwell equations in which the electric field strength and magnetic field strength are coupled. Because the concentration of dielectric sources due to ferromagnetic materials in concrete is usually negligible (Li et al. 1993), the electromagnetic wave generation inside concrete may be neglected, which means that the Maxwell equations become decoupled (von Hippel 1954);

$$\nabla^2 \mathbf{E} = \epsilon \mu \frac{\partial^2 \mathbf{E}}{\partial t^2} \quad (2a)$$

and

$$\nabla^2 \mathbf{H} = \epsilon \mu \frac{\partial^2 \mathbf{H}}{\partial t^2} \quad (2b)$$

The transverse electromagnetic waves may be considered to be parallel, and their incidence to the concrete surface to be normal.

Therefore, aside from time  $t$ , the dielectric field depends only on coordinate  $x$  normal to the surface [Fig. 1(b)]. Eqs. (2a) and (2b) are simply solved as

$$\mathbf{E} = \mathbf{E}_0 e^{i\omega t - \gamma x} \quad (3a)$$

and

$$\mathbf{H} = \mathbf{H}_0 e^{i\omega t - \gamma x} \quad (3b)$$

where  $\gamma$  = complex propagation factor.

At the interface of two different media, the electromagnetic wave is partially reflected and partially transmitted as a refracted wave. The magnitude of refracted wave is given by Fresnel's equation, and the reflection and refraction angles by Snell's law (e.g., von Hippel 1954). If the wave is incident to the interface of two dielectric media in normal direction, the wave forms a standing wave pattern. Since only a normal incidence is considered here, the wave can be calculated simply from the continuity condition at each interface (e.g., Cheng 1983; Wait 1985).

Consider the concrete wall, sketched in Fig. 1(b), to be subdivided into parallel strips normal to the surface which either contain steel reinforcement or not [Fig. 1(d)]. Medium 0 represents air and media  $k = 1, 2, \dots, M$  the layers of concrete with different water contents [Fig. 1(b)]. Medium  $M + 1$  represents air in the case of unreinforced strips, or steel in the case of reinforced strips in Fig. 1(d). By analogy with the transmission line theory (which is used to calculate the voltage and current in an electric circuit), the wave solutions in medium  $k$  are obtained as follows (Wait 1985):

$$E(x) = C_k (e^{-\gamma_k x} + R_k e^{\gamma_k x})$$

and

$$H(k) = (C_k / \eta_k) (e^{-\gamma_k x} - R_k e^{\gamma_k x}) \quad \text{for } 0 < x < l \quad (4)$$

where  $C_k$  = transmission factor;  $R_k$  = reflection factor; and  $\eta_k$  = intrinsic impedance of medium  $k$ . Here  $\eta_k = \gamma_k / i\omega\epsilon_k = \sqrt{\mu_k / \epsilon_k}$ . The transmission factor of air is given as the initial electric strength  $E_0$ . The reflection factor between air and the first concrete layer is denoted as  $R_0$

$$R_0 = (Z_1 - \eta_0) / (Z_1 + \eta_0) \quad (5)$$

where  $Z_1$  = transmission impedance of medium 1. The impedance of medium  $k$  is obtained from the transmission line theory as

$$Z_k = \eta_k (Z_{k+1} + \eta_k \tanh \gamma_k l_k) / (\eta_k + Z_{k+1} \tanh \gamma_k l_k) \quad (6)$$

$$Z_{M+1} = \eta_k (\eta_{M+1} + \eta_M \tanh \gamma_M l_M) / (\eta_M + \eta_{M+1} \tanh \gamma_M l_M) \quad (7)$$

where  $l_k = x_k - x_{k-1}$  = width of each layer. For unreinforced strips,  $\eta_{M+1} = \eta_0$ . For reinforced strips,  $\eta_{M+1} = 0$ , which implies an almost 100% reflection by reinforcing bars. From the condition of continuity at each interface,  $R_k$  and  $C_k$  are obtained as follows:

$$R_k = e^{-2\gamma_k x_{k-1}} [E_{k-1}(x_{k-1}) - H_{k-1}(x_{k-1}) \eta_k] / [E_{k-1}(x_{k-1}) + H_{k-1}(x_{k-1}) \eta_k] \quad (8)$$

$$C_k = [E_{k-1}(x_{k-1})] / [e^{-\gamma_k x_{k-1}} + R_k e^{\gamma_k x_{k-1}}] \quad (9)$$

As we have seen, the solution of the electric field strength  $E_k$  of medium  $k$  [Fig. 1(b)] [Fig. 1(b), Eq. (4)] is a complex function. The real part of  $E_k$  is taken as the actual solution. The rate of volumetric heat generation by the transverse electromagnetic waves can be obtained from Eq. (1). Because the wave period  $T = 1/f$  is far shorter than the time that the thermal heat front takes

to advance through one wavelength of the electromagnetic wave, it is meaningful to average the heat generation rate over period  $T$ ;

$$I_{(h)}^{\text{ave}} = \frac{1}{T} \int_0^{T=2\pi/\omega} \sigma [\text{Re}(E)]^2 dt \quad (10)$$

$$= \frac{1}{2} \sigma \|C\|^2 \{e^{-2\alpha x} + \|R\|^2 e^{2\alpha x} + [R' \cos 2\beta x - R'' \sin 2\beta x]\} \quad (11)$$

where  $C = C' + iC''$  = transmission factor;  $R = R' + iR''$  = reflection factor;  $\beta$  = phase factor; and  $\alpha$  = attenuation factor ( $1/\alpha$  represents the depth through which the field strength decays to  $1/e = 0.368$  of its original value); here  $\gamma = \sqrt{i\mu\omega(\sigma + i\epsilon\omega)} = \alpha + i\beta$  = complex propagation factor.

A typical layout of a reinforced concrete wall is depicted in Fig. 1(c). The wave is reflected and scattered by steel reinforcing bars as well as the aggregates. Although the arrangement of the bars is three dimensional, they may be approximately treated one dimensionally and thus their location will be characterized just by the depth  $d$  below the surface (Fig. 1). Therefore, due to the heterogeneity of concrete wall, we may take the spatial average of Eq. (11) over the wave number  $2\pi/\beta$ . As a result, the averaged heat generation rate is obtained as

$$I_{(h)} = \frac{1}{2} \sigma \|C\|^2 (e^{-2\alpha x} + \|R\|^2 e^{2\alpha x}) \quad (12)$$

Note that, when the second term, which represents power reflection by rebars, is neglected, Eq. (13) becomes the well-known Lambert's law:

$$I_{\text{Lambert}} = I_0 e^{-2\alpha x} \quad (13)$$

where  $I_0$  = heat generation rate at the surface. The advantage of Lambert's law, which is widely used in low-temperature food engineering (Metaxas and Meredith 1983; Taoukis et al. 1987; Meredith 1998), is that it is simple and easy to understand.

## Effect of Reinforcing Bars on Microwave Penetration

As an approximation, the reinforced concrete may be considered for our purposes as a parallel combination of unreinforced and reinforced strips in the direction normal to surface, labeled by subscripts  $U$  and  $R$ ; Fig. 1(d). The overall average volumetric heat generation in the reinforced concrete wall can be obtained as the average of the heat generations in two adjacent strips

$$I_{(h)} = \begin{cases} (1-p)I_U + pI_R & \text{for } x < d \\ (1-p)I_U & \text{for } x \geq d \end{cases} \quad (14)$$

where  $p$  = area fraction of the steel reinforcing bars on a plane parallel to concrete surface; and  $I_U$ ,  $I_R$  = rate of heat generation in unreinforced and reinforced strips normal to surface, respectively. Both  $I_U$  and  $I_R$  are obtained from Eq. (13). Note that, because of different boundary conditions, the electric strength of  $E_U$  is different from  $E_R$ ; it is assumed that  $E_U$  is transmitted into air at the opposite surface of the wall, and  $E_R$  is perfectly reflected at the location of the steel bars  $d$ .

For the sake of simplicity, the foregoing analysis neglects calculation of the three-dimensional diffraction and scattering of the electromagnetic waves due to steel bars. The diffraction and scattering are surely much less significant than the wave reflection, because of the steep power decay in the concrete cover (see Part II).

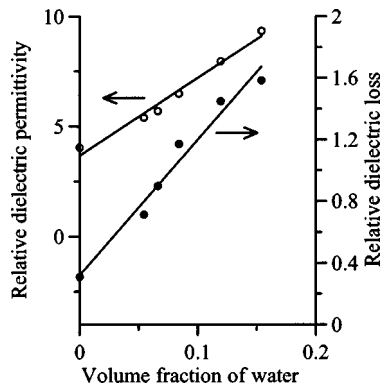


**Fig. 2.** Relative dielectric properties of concrete depending on water content (Hasted and Shah 1964)

### Dielectric Properties of Concrete

The properties of dielectric materials generally depend on moisture contents and temperature changes (Metaxas and Meredith 1983). The relative dielectric permittivity  $\kappa' = \epsilon' / \epsilon_0$  and the relative dielectric loss  $\kappa'' = \epsilon'' / \epsilon_0$  of concrete quadratically increase as a function of volume fraction of water  $v_w$  (Hasted and Shah 1964; Shah et al. 1965) ( $\epsilon_0$  = dielectric permittivity of air =  $8.86 \times 10^{-12}$  F/m). The dielectric constants  $\kappa'$  and  $\kappa''$  change significantly when  $v_w$  exceeds about 20%. When  $v_w$  is less than 20%, the changes can be approximated by linear functions (Fig. 2). The concretes that need to be decontaminated are usually old concretes, in which the volume fraction of water is around 7%. Because the water content is a function of pore pressure and temperature, as described by the constitutive laws [Eq. (17)], the dielectric properties of concrete depend not only on the water content but also, indirectly, on temperature. Regarding a direct effect of temperature on the dielectric properties, no information is available and probably this effect is negligible.

### Application of Microplane Constitutive Model M4

To determine whether a given microwave source will achieve spalling and predict the depth of spalling, a good constitutive model relating the stress and strain in concrete is needed. Li et al. (1993) considered a restrained one-dimensional elastic bar and estimated its stress simply as  $\sigma = -E\alpha\Delta T$ . This estimate, however, ignores the nonlinearity of deformation on approach to spalling and the confining effect of the body surrounding a hot spot heated by microwaves. A three-dimensional constitutive model needs to be used.

For this purpose, version M4 of the microplane model (briefly described in Appendix III of Part II) has been adopted (Bažant et al. 2000b; Caner and Bažant 2000). The microplane model is a powerful explicit model that yields the best data fit over broad range of nonlinear triaxial behavior, softening damage and tensile cracking of concrete (Bažant et al. 2000b; Caner and Bažant 2000). Fracture propagation can be handled with model M4 most easily in the sense of the crack band model.

The microplane model differs from the classical tensorial models based on plasticity by the fact that the constitutive law is expressed in terms of vectors rather than tensors. The vectors are the stress and strain vectors on planes of all possible orientations within the material. Thanks to all possible microplane orientations, the model automatically satisfies tensorial invariance con-

ditions. The strain vectors on the microplanes are assumed to be the projections of the continuum strain tensor, and the stress tensor is related to the microplane stress vectors through a variational principle. For a detailed description of the microplane model and the history of development, with a literature review, see Bažant et al. (2000b), and for various related aspects also Brocca and Bažant (2000).

### Thermal Degradation of Concrete

Besides the triaxial and strain softening behavior, concrete also undergoes thermal degradation and transient creep. Both the compressive strength  $f_c$  and the Young's modulus  $E$  degrade as the temperature increases. The degradation is typically determined from tests of the residual mechanical properties of concrete exposed for some time [typically 12 h, (Felicetti and Gambarova 1998)] to various controlled temperature histories. The surface temperature, as calculated in Part II of this study (Zi and Bažant 2003), reaches less than 400°C during the 10 s of heating envisaged for decontamination. If this temperature were sustained for many hours, the compressive strength of concrete would degrade to about 85% of the original value (Bažant and Chern 1987). But what if this temperature lasts for only 10 s?

The degradation is caused by dehydration of the calcium silicate hydrates in cement paste. Since the chemical reactions of dehydration at high temperature cannot happen instantly and probably take much longer than the desired 10 s duration of the decontamination process, the degradation will be neglected.

The temperature increase near 400°C will intensify creep as well as the apparent effect of strain rate on the elastic modulus of concrete. This could be taken into account by introducing on the microplanes a creep law based on the Maxwell or Kelvin chain (Zi and Bažant 2001). According to finite element simulations, the maximum strain rate in the heated concrete prior to spalling, which occurs near the surface, is about  $\dot{\epsilon} = 1 \times 10^{-4} \text{ s}^{-1}$ . Compared to the typical loading rate in quasi-static laboratory tests, which is about  $5 \times 10^{-6} \text{ s}^{-1}$ , the rate effect would increase the apparent Young's modulus to approximately 120% (Bažant et al. 2000a) of the normal value, but only near the place of maximum strain rate. Elsewhere the rate effect will be significantly less. The rate effect will be neglected in the present finite element computations.

It might seem that the rate effect might get offset somewhat by the effect of thermal degradation. However, thermal degradation is a far slower process (Ulm et al. 1999), which is surely negligible within the duration of 10 s.

### Hygrothermal Strain

The thermal expansion coefficient  $\alpha_T$  of cement mortar changes significantly with temperature, which is caused by moisture effects. But for concrete, the change of  $\alpha_T$  with temperature is much less pronounced. This is explained by the restraining effect of aggregates in concrete, which are usually very stable chemically (Harmathy 1970; Bažant and Kaplan 1996; Neville 1997). Therefore the thermal expansion coefficient  $\alpha_T$  will simply be taken as constant ( $\approx \alpha_T = 10.0 \times 10^{-6} \text{ K}^{-1}$ ) in the temperature range of the decontamination process. Thus the strain rate  $\dot{\epsilon}_T$  due to thermal dilatation is expressed as

$$\dot{\epsilon}_T = \alpha_T \dot{T}$$

Regarding shrinkage, two kinds must be distinguished: (1) the average shrinkage of the cross section of a concrete member, which is not a constitutive property but a property of the whole cross section, with an inevitably complex mathematical description (Hansen and Almudaiheem 1987; ACI 1994; Bažant and Baweja 1995; Bažant and Baweja 2000); and (2) the shrinkage at a point of the continuum approximating concrete, which is a constitutive property. Unfortunately, the latter is next to impossible to measure directly (direct measurements have been made only on cement paste shells 0.75 mm in thickness, which is the maximum thickness needed to ensure that the humidity profile across the wall would remain almost uniform during a programmed linear decrease of environmental relative humidity at the rate 3%/h; Bažant and Najjar 1972).

Therefore the constitutive shrinkage of the material had to be inferred indirectly—by fitting the finite element solutions of test specimens to the measured deformations and adjusting the shrinkage model until a good fit is obtained (Bažant and Chern 1987; Bažant and Xi 1994; Bažant et al. 1997). The conclusion from these studies is very simple:

$$\dot{\epsilon}_h = \kappa_s \dot{h}$$

where  $\kappa_s$  = shrinkage coefficient (taken as  $\kappa = 0.5 \times 10^{-3}$ , according to model B3; Bažant and Baweja 2000).

## Conclusions

1. The paper presents a mathematical formulation for analyzing a proposed technique of decontamination of concrete walls from radionuclides residing in a thin surface layer, which is to be spalled off by rapid microwave heating. The formulation consists of (1) a model for heat generation in the bulk of concrete by microwave power dissipation; (2) a model for heat and moisture transfer with buildup of pore pressure; (3) a constitutive model for nonlinear triaxial behavior and fracturing of concrete; and (4) numerical solution.
2. The heat and moisture transfer is based on the model of Bažant and Thonguthai (1978), which is improved by introducing a more realistic rapid increase of the magnitude of the moisture permeability upon exceeding 100°C. An ohmic heat source term representing the rate of heat generation by microwaves is included in the formulation.
3. A simple analytical expression for the heat generation rate is developed. The heat generation rate caused by normally incident transmission electron microscopy waves is averaged over both the frequency and the wavelength. The microwave power reflection by steel reinforcing bars is taken into account in the resulting formula. The special case for no reinforcement agrees with the Lambert's law used in food engineering. The heat generation rates are determined separately for two kinds of strips normal to wall surface: one representing an unreinforced concrete and the other a concrete containing reinforcement bars at which the microwave is 100% reflected.
4. The recently developed version M4 of microplane model for concrete is adopted for the analysis of stresses and fracturing. Shrinkage and swelling due to changes in water content are taken into account, but creep is neglected because the duration of the spalling process is very short (only about 10 s).

## Appendix: Heat and Moisture Transfer in Concrete

### Governing Equations

The mass conservation equation and heat conservation equation are

$$\frac{\partial w}{\partial t} + \nabla \cdot \mathbf{J} = I_{(w)} \quad (15a)$$

and

$$\frac{\partial}{\partial t} (\rho C T) + \nabla \cdot \mathbf{q} = I_{(h)} \quad (15b)$$

Here  $\nabla$  = gradient operator;  $T$  = temperature;  $\rho$  = mass density of concrete;  $C$  = specific heat of concrete;  $w$  = specific water content;  $C_w$  = specific heat of water;  $\mathbf{J}$  = water flux vector;  $\mathbf{q}$  = conductive heat flux vector;  $I_{(h)}$  = distributed source of heat; and  $I_{(w)}$  = distributed source of water, due to release of chemically bound water (Bažant and Thonguthai 1978; Bažant and Kaplan 1996); subscripts  $(w)$  and  $(h)$  are labels for water and heat.

The heat capacity of oven dried concrete can be used for  $C$  since the latent heat due to heating induced chemical decomposition of hydrates in cement paste is relatively small, and negligible for concrete (Harmathy and Allen 1973), due to its large volume fraction of aggregates. Although the apparent heat capacity of concrete depends on the water content, the mass fraction of water is usually so small (less than 6% of total mass of concrete, even at saturation) that this dependence may be neglected, for simplicity (Bažant and Thonguthai 1978).

The water flux  $\mathbf{J}$  and the heat flux  $\mathbf{q}$  may be expressed in terms of the gradient of water content  $w$  and the gradient of temperature  $T$ , respectively

$$\mathbf{J} = -\frac{a}{g} \nabla P \quad (16a)$$

and

$$\mathbf{q} = -k \nabla T \quad (16b)$$

where  $a$  = permeability;  $g$  = gravity acceleration;  $P$  = pore pressure; and  $k$  = heat conductivity. Heat is also transferred by the movement of water inside of concrete, which is described by the convection term  $\mathbf{q}_{cv} = C_w T \mathbf{J}$ . In concrete, however, this term is negligible, because the diffusivity to pore water is about 3 orders of magnitude smaller than the heat diffusivity.

### Equation of State of Pore Water

Except for temperatures above the critical point of water (374.15°C), one must distinguish the vapor from the liquid water in the pores of concrete. These two phases of water can be assumed to be locally always in thermodynamic equilibrium. Bažant and Thonguthai's (1978, 1979) model based on this hypothesis was shown to give acceptable match of the test data. Because of the complexity of the pore system, and especially the role of water adsorbed in the nanopores of hydrated cement paste, the formulation of the sorption isotherms of concrete, i.e., the curves of specific water content  $w$  versus relative humidity of water vapor in the pores,  $h = P/P_s(T)$  [where  $P_s(T)$  = saturation pore pressure at temperature  $T$ ], must be semiempirical. The isotherms are described as

$$\frac{w}{c} = \left( \frac{w_1}{c} h \right)^{1/m(T)} \quad \text{for } h \leq 0.96 \quad (17a)$$

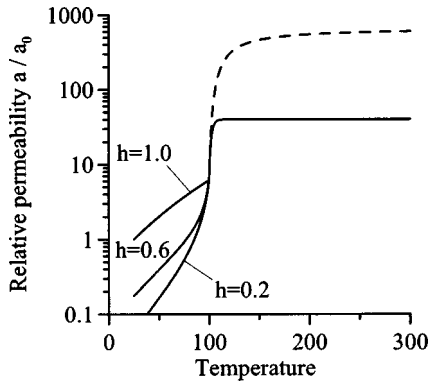


**Fig. 3.** Change of permeability by change of humidity and temperature

and

$$w = (1 + 3\varepsilon_v)n/v \text{ for } h \geq 1.04 \quad (17b)$$

where  $T$  = temperature in  $^{\circ}\text{C}$ ;  $T_0 = 25^{\circ}\text{C}$ ;  $c$  = mass of anhydrous cement per unit volume of concrete;  $w_1$  = saturation water content at reference temperature  $T_0$  ( $=25^{\circ}\text{C}$ );  $m(T) = 1.04 - [T'/(22.34 + T')]$ ;  $T' = (T + 10)/(T_0 + 10)^2$ ;  $d\varepsilon_v = d\sigma_v/(3K) + \alpha_T dT$ ;  $\sigma_v = nP$ ;  $\varepsilon_v$  = linear volumetric strain;  $K$  = bulk modulus of concrete;  $n$  = porosity accessible to water;  $v = v(T, P)$  = specific volume of water; and  $\alpha_T$  = coefficient of linear thermal dilatation of concrete. The porosity (pore volume accessible to water), which was estimated from considerations of weight loss, is expressed as  $n = [n_0 + \rho_0^{-1}w_d(T)]\psi(h)$  for  $h \geq 1.04$ , where  $n_0$  = reference porosity at  $25^{\circ}\text{C}$ ;  $w_d(T)$  = weight loss [obtained from thermogravimetric measurements (Harmathy and Allen 1973)];  $\rho_0$  = specific weight of water; and  $\psi(h) = 1 + 0.12(h - 1.04)$ .

### Permeability and Conductivity

The permeability of concrete is a complex property. Because the capillaries in good quality concretes are not continuous, water molecules must pass through the nanopores in the hardened cement paste. Because the width of such pores (from 0.5 nm up) is much smaller than the mean free path of vapor molecules (about 80 nm at  $25^{\circ}\text{C}$ ), water molecules cannot pass through the nanopores in a vapor state but must become adsorbed on the pore walls and migrate along adsorption layers. So the nanopores control the permeability, which explains the extremely low values of the permeability of concrete at normal temperatures. But this is not the case at high temperatures. When the temperature is increased above  $100^{\circ}\text{C}$ , the permeability jumps sharply up (Bažant and Thonguthai 1978). This can be explained by heat-induced changes in the structure of the smallest pores, particularly elimination of the narrowest necks, of nanometer dimensions, on the passages through cement paste. Based on data fitting, the permeability was inferred to jump up about  $200\times$ , but the present optimum fits of test data shown later indicates that the permeability jumps up, around  $100^{\circ}\text{C}$ , only about  $6.5\times$  (Fig. 3). The initial trend of function  $f_3(T)$ , which represents the permeability increase upon exceeding  $100^{\circ}\text{C}$ , is the same as proposed in Bažant and Thonguthai's (1978) work, but the magnitude of the jump needs to be scaled down, as represented by the following function:

$$a = a_0 f_1(h) f_2(T) \text{ for } T \leq 100^{\circ}\text{C} \quad (18a)$$

and

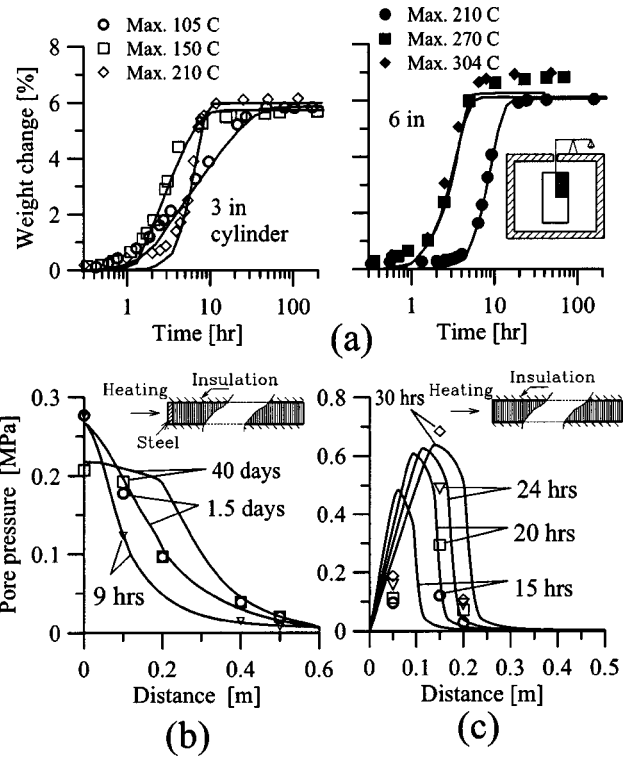


**Fig. 4.** Fits of (a) Bažant and Thonguthai's experiments (1978); (b) England and Ross' experiments (1970); and (c) by model proposed; symbols represent experimental data and solid lines represent fitting

$$a = a_0 f_2(100) f_3(T) \text{ for } T > 100 \quad (18b)$$

where  $a_0$  = reference permeability at  $25^{\circ}\text{C}$ . Function  $f_1(h)$  characterizes the permeability corresponding to moisture transfer along the adsorbed water layers. The temperature dependence of permeability below  $100^{\circ}\text{C}$  is given by an Arrhenius-type equation  $f_2(h)$ ;

$$f_1(h) = \alpha + \frac{1 - \alpha}{1 + \left(\frac{1-h}{1-h_c}\right)^4}, \text{ for } h \leq 1; f_1(h) = 1, \text{ for } h \geq 1 \quad (19)$$

$$f_2(T) = \exp\left[\frac{Q}{R}\left(\frac{1}{\bar{T}_0} - \frac{1}{\bar{T}}\right)\right] \quad (20)$$

where  $\alpha = 1/[1 + 0.253(100 - \min(T, 100^{\circ}\text{C}))]$ ;  $h_c = 0.75$ ,  $\bar{T}$  = absolute temperature;  $Q$  = activation energy for water migration; and  $R$  = gas constant. Based on data fitting, the value  $Q/R = 2,700$  K was recommended (Bažant and Najjar 1972). Function  $f_3(T)$ , which describes the abrupt increase of permeability near  $100^{\circ}\text{C}$ , is revised as

$$f_3(T) = 5.5 \left\{ \frac{2}{1 + \exp[-0.455(T - 100)]} - 1 \right\} + 1 \quad (21)$$

which is found by fitting the data used in Bažant and Thonguthai (1978), England and Ross (1970), and Zhukov and Schenchenko (1974) (Fig. 4).

The thermal conductivity of cement, too, depends on the changes of temperature and moisture content significantly. However, the thermal conductivity  $k$  is for concrete is much less sensitive to the changes of temperature and moisture than it is for the

hardened cement paste and concrete. The reason for this difference is that the mineral aggregates, which represent most of the volume of concrete and are usually chemically stable materials (Harmathy 1970), conduct heat no less than the cement paste but do not transfer moisture significantly. In general, the thermal conductivity depends on the volume fraction of aggregate and its type (Bažant and Kaplan 1996; Neville 1997).

### Distributed Sources of Water and Heat

When concrete is heated, the chemically bound water becomes free and gets released into the pores. This is reflected in the source term  $I_{(w)}$  of the mass conservation condition in Eq. (15). The amount of dehydrated water is obtained experimentally, by weight loss measurements;  $w_d(T) = w_h^{105} f_d(T)$ , where  $w_h^{105}$  = the hydrate water content at 105°C. The values of  $f_d(T)$  are interpolated using the experimental data by Harmathy and Allen (1973). At temperatures below 100°C, the phenomenon must be reversed because of further hydration of cement. The increase of the hydrate water content  $w_h$  below 100°C may be described as  $w_h(t_e) \approx 0.21c[t_e/(\tau_e + t_e)]^{1/3}$ , where  $t_e$  = equivalent hydration period and  $\tau_e = 23$  days (see Bažant and Kaplan 1996). Then the distributed water source is  $I_{(w)} = \dot{w}_d - \dot{w}_h$ .

The distributed heat source term in Eq. (15b) is absent when concrete is heated by conduction from the surface. But when concrete is heated by microwaves, the heat source, Eqs. (13) and (14), generated by ohmic heat dissipation within the concrete volume, is significant.

### Boundary Conditions

Heat and mass are transferred at the surface to the surrounding environment. Physically accurate modeling of the environment near the surface, which would call for nonlinear hydrodynamics, is not necessary. For heat transfer, it suffices to use Newton's law of cooling (e.g., Chapman 1987) and a similar law for moisture transfer. Thus the boundary conditions simply are

$$\mathbf{n} \cdot \mathbf{J} = B_w(P_s - P_{am}), \quad (22a)$$

and

$$\mathbf{n} \cdot \mathbf{q} = B_T(T_s - T_{am}) \quad (22b)$$

where  $B_w$  = moisture transfer coefficient and  $B_T$  = heat transfer coefficient;  $\mathbf{n}$  = unit outward normal of the boundary surface;  $P_{am}$  = ambient partial pressure of water vapor;  $T_{am}$  = ambient temperature;  $P_s$  = partial vapor pressure at the surface (i.e., in the capillary pores adjacent to the surface); and  $T_s$  = surface temperature. A perfectly sealed (or insulated) surface is a limiting case for  $B_w = 0$  (or  $B_T = 0$ ), and perfect moisture transmission (or heat transmission) is a limiting case for  $B_w \rightarrow \infty$  (or  $B_T \rightarrow \infty$ ). In the case of free convection of air near the surface,  $B_T$  is in the range of 5–25 J/m<sup>2</sup> s°C (e.g., Chapman 1987) and  $B_w \approx \infty$  (Bažant and Thongthai 1978).

The heat radiation from the surface, which is the only mechanism of heat loss in a vacuum, is described by Stefan's radiation law

$$\mathbf{n} \cdot \mathbf{q}_r = \gamma \sigma (T_s^4 - T_{am}^4) \quad (23)$$

where  $\mathbf{q}_r$  = radiation heat flux;  $\sigma$  = Stefan coefficient =  $5.67 \times 10^{-8}$  J/m<sup>2</sup> s K<sup>4</sup>; and  $\gamma$  = heat emissivity, which varies in the range of 0–1. For a perfectly black surface,  $\gamma = 1$ , while for brick,  $\gamma = 0.9$  (Jones 2000); because of lack of data, and also because the precise value is not very important, the same emissivity  $\gamma$  as

for brick is assumed for concrete. In the absence of vacuum, both the surface heat transfer, Eq. (22), and the radiation, Eq. (23), take place simultaneously. They may be conveniently characterized as

$$\mathbf{n} \cdot \mathbf{q} = B_{eq}(T_s - T_{am}) \quad (24)$$

where  $B_{eq}$  = equivalent heat transfer coefficient =  $B_T + \gamma \sigma (T_s^2 + T_{am}^2)(T_s + T_{am})$ .

### Why Not Liquid–Gas Transport Model?

One might wonder why the recent model of Mainguy et al. (2001), or some other multiphase transport model, has not been adopted. In that model, all the mobile water is assumed to consist of liquid (capillary) water and water vapor contained in the gas (air), the pressure gradient of which is regarded as one driving force of transport. From this starting hypothesis, it is deduced that the water transport is controlled by the flow of liquid (capillary) water and involves evaporation and condensation at gas-liquid interfaces. The starting hypothesis, however, ignores the fact that the capillaries in normal hardened cement paste are not continuous (unless the water-cement ratio were abnormally high). While diffusing, the water molecules must pass through nanopores in calcium silicate hydrates only about 1–3 nm wide, which cannot contain liquid water and thus cannot allow its passage. Moreover, since the mean free path of water molecules in a vapor phase is about 80 nm, there is no chance of vapor molecule passage through the tortuous nanopores (they would bounce off pore walls far more often than of each other, and have about equal chance to be reflected forward or backward). Therefore, water molecules can move through such passages only along adsorption layers which fill these pores. Such water transport is controlled not by viscosity of liquid water, but by the lingering times of the adsorbed water molecules on the surface of calcium silicate hydrates (Bažant 1972, 1975). For these reasons, the theory of Mainguy et al. (2001) and numerous other multiphase transport theories are not applicable (the separation of transport of air in Mainguy et al.'s model might be relevant, although this has not been worked out).

### References

- Ahmed, G. N., and Hurst, J. P. (1997). "Coupled heat and mass transport phenomena in siliceous aggregate concrete slabs subjected to fire." *Fire Mater.*, 21, 161–168.
- American Concrete Institute. (ACI). (1994). "Prediction of creep, shrinkage, and temperature effects in concrete structures." *ACI manual of concrete practice Part 1: Materials and general properties of concrete*, ACI 209R-92, Detroit.
- Bažant, Z. P. (1972). "Thermodynamics of interacting continua with surfaces and creep analysis of concrete structures." *Nucl. Eng. Des.*, 20, 477–505.
- Bažant, Z. P. (1975). "Theory of creep and shrinkage in concrete structures: A precis of recent developments." *Mechanics today*, S. Nemat-Nasser, ed., Vol. 2, Pergamon, New York, 1–93.
- Bažant, Z. P., and Baweja, S. (1995). "Justification and refinement of Model B3 for concrete creep and shrinkage. 1. Statistics and sensitivity." *Materials and structures*, Vol. 28, RILEM, Paris, 415–430.
- Bažant, Z. P., and Baweja, S. (2000). "Creep and shrinkage prediction model for analysis and design of concrete structures: Model B3—short form." *Adam Neville Symposium: Creep and shrinkage—structural design effects*, ACI SP-194, A. Al-Manaseer, ed., American Concrete Institute, Farmington Hills, Mich., 85–100.
- Bažant, Z. P., Caner, F. C., Adley, M. D., and Akers, S. A. (2000a). "Fracture rate effect and creep in microplane model for dynamics." *J. Eng. Mech.*, 126(9), 962–970.

- Bažant, Z. P., Caner, F. C., Carol, I., Adley, M. D., and Akers, S. A. (2000b). "Microplane model M4 for concrete I: Formulation with work-conjugate deviatoric stress." *J. Eng. Mech.*, 126(9), 944–953.
- Bažant, Z. P., and Chern, J. (1987). "Stress-induced thermal and shrinkage strains in concrete." *J. Eng. Mech.*, 113(10), 1493–1511.
- Bažant, Z. P., Hauggaard, A. B., Baweja, S., and Ulm, F. (1997). "Microprestress-solidification theory for concrete creep. I: Aging and drying effects." *J. Eng. Mech.*, 123(11), 1188–1194.
- Bažant, Z. P., and Kaplan, M. F. (1996). *Concrete at high temperatures*, Longman, London.
- Bažant, Z. P., and Najjar, L. J. (1972). "Nonlinear water diffusion in nonsaturated concrete." *Materials and Structures*, Vol. 5, RILEM, Paris, 3–20.
- Bažant, Z. P., and Thonguthai, W. (1978). "Pore pressure and drying of concrete at high temperature." *J. Eng. Mech. Div., Am. Soc. Civ. Eng.*, 104(5), 1059–1079.
- Bažant, Z. P., and Thonguthai, W. (1979). "Pore pressure in heated concrete walls: Theoretical prediction." *Mag. Concrete Res.*, 31(107), 67–76.
- Bažant, Z. P., and Xi, Y. (1994). "Drying creep of concrete: constitutive model and new experiments separating its mechanisms." *Mater. Struct.*, 27, 3–14.
- Bažant, Z. P., and Zi, G. (2001). "Spatial and temporal scaling of concrete response to extreme environments." *Proc., 3rd Int. Conf., Concrete Under Severe Conditions*, N. Banthia, K. Sakai, and O. E. Gjörv, eds., Univ. of British Columbia, Vancouver, BC, 3–10.
- Brocca, M., and Bažant, Z. P. (2000). "Microplane model and metal plasticity." *Appl. Mech. Rev.*, 53(10), 265–281.
- Caner, F. C., and Bažant, Z. P. (2000). "Microplane model M4 for concrete II: Algorithm and calibration." *J. Eng. Mech.*, 126(9), 954–961.
- Chapman, A. J. (1987). *Fundamentals of heat transfer*, Macmillan, New York.
- Cheng, D. K. (1983). *Field and wave electromagnetics*, Addison-Wesley, London.
- England, G. L., and Ross, A. D. (1970). "Shrinkage, moisture and pore pressure in heated concrete." *Proc., American Concrete Institute Int. Seminar on Concrete for Nuclear Reactors*, West Berlin, Germany, Special Publication No. 34, 883–907.
- Felicetti, R., and Gambarova, G. (1998). "Effects of high temperature on the residual compressive strength of high siliceous concretes." *ACI Mater. J.*, 95(4), 395–406.
- Gawin, D., Majorana, C. E., and Schrefler, B. A. (1999). "Numerical analysis of hygrothermal behaviour and damage of concrete at high temperature." *Mech. Cohesive-Frict. Mater.*, 4, 37–74.
- Hansen, W., and Almudaihem, J. A. (1987). "Ultimate drying shrinkage of concrete—Influence of major parameters." *ACI Mater. J.*, 84(3), 217–223.
- Harmathy, T. Z. (1970). "Thermal properties of concrete at elevated temperature." *J. Mater.*, 5(1), 47–75.
- Harmathy, T. Z., and Allen, L. W. (1973). "Thermal properties of selected masonry unit concrete." *ACI J.*, 70(15), 132–142.
- Hasted, J. B., and Shah, M. A. (1964). "Microwave absorption by water in building materials." *Br. J. Appl. Phys.*, 15, 825–836.
- Hertz, K. (1981). "Microwave heating for fire material testing of concrete—A theoretical study," *Institute of Building Design Rep. No. 144*, Technical Univ. of Denmark, Lyngby, Denmark.
- Hertz, K. (1983). "Microwave heating for fire material testing of concrete—an experimental study." *Institute of Building Design, Rep. No. 164*, Technical Univ. of Denmark, Denmark.
- Jones, H. R. N. (2000). *Radiation heat transfer*, Oxford University Press, Oxford.
- Lagos, L. E., Li, W., and Ebadian, M. A. (1995). "Heat transfer within a concrete slab with a finite microwave heating source." *Int. J. Heat Mass Transf.*, 38(5), 887–897.
- Li, W., Ebadian, M. A., White, T. L., and Grubb, R. G. (1993). "Heat transfer within a concrete slab applying the microwave decontamination process." *J. Heat Transfer*, 115, 42–50.
- Mainguy, M., Coussy, O., and Baroghel-Bouny, V. (2001). "Role of air pressure in drying of weakly permeable materials." *J. Eng. Mech.*, 127(6), 582–592.
- Meredith, R. J. (1998). *Engineer's handbook of industrial microwave heating*, The Institution of Electrical Engineers, London.
- Metaxas, R. C., and Meredith, R. J. (1983). *Industrial microwave heating*, IEEE Power Engineering Series 4, Peter Peregrinus Ltd., Exeter, England.
- Moukwa, M., Brodwin, M., Christo, S., Chang, J., and Shah, S. P. (1991). "The influence of the hydration process upon microwave properties of cements." *Cem. Concr. Res.*, 21, 863–872.
- Neville, A. M. (1997). *Properties of concrete*, 4th Ed, Wiley, New York.
- Shah, M. A., Hasted, J. B., and Moore, L. (1965). "Microwave absorption by water in building materials: Aerated concrete." *Br. J. Appl. Phys.*, 16, 1747–1754.
- Spalding, B. (2000). "Volatility and extractability of Strontium-85, Cesium-134, Cobalt-57, and Uranium after heating hardened portland cement paste." *Environ. Sci. Technol.*, 34, 5051–5058.
- Taoukis, P., Davis, E. A., Davis, H. T., Gordon, J., and Talmon, Y. (1987). "Mathematical modeling of microwave thawing by the modified isotherm migration method." *J. Food. Sci.*, 52(2), 455–463.
- Thuéry, J. (1992). *Microwaves: industrial, scientific, and medical applications*, Artech House, Boston, 104.
- Ulm, F.-J., Coussy, O., and Bažant, Z. P. (1999). "The "chunnel" fire I: chemoplastic softening in rapidly heated concrete." *J. Eng. Mech.*, 125(3), 272–282.
- Vodák, F., Černý, R., Drchalová, J., Hošková, Š., Kaptčková, O., Michalko, O., Semerák, P., and Toman, J. (1997). "Thermophysical properties of concrete for nuclear-safety related structures." *Cem. Concr. Res.*, 27(3), 415–426.
- von Hippel, A. R. (1954). *Dielectric materials and applications*, MIT Press, Cambridge, Mass.
- Wace, P. F., Harker, A. H., and Hills, D. L. (1989). "Removal of concrete layers from biological shield by microwaves." *Rep. No. EUR 12185*, Nuclear Science and Technology, Commission of the European Communities, Brussels, Belgium.
- Wait, J. R. (1985). *Electromagnetic wave theory*, Harper & Row, New York.
- Watson, A. (1968a). "Curing of concrete." *Microwave power engineering*, E. C. Okress, ed., Vol. 2, Academic, New York.
- Watson, A. (1968b). "Breaking of concrete." *Microwave power engineering*, E. C. Okress, ed., Vol. 2, Academic, New York.
- Wei, C. K., Davis, H. T., Davis, E. A., and Gordon, J. (1985). "Heat and mass transfer in water-laden sandstone: microwave heating." *AIChE J.*, 31(5), 842–848.
- White, T. L., Foster, D., Jr., Wilson, C. T., and Schaich, C. R. (1995). "Phase II microwave concrete decontamination results." *ORNL Rep. No. DE-AC05-84OR21400*, Oak Ridge National Laboratory, Oak Ridge, Tenn.
- Zhukov, V. V., and Schenchenko, V. I. (1974). "Investigation of causes of possible spalling and failure of heat-resistant concretes at drying, first heating and cooling." *Zharostoikie betony (Heat-resistant concretes)*, K. D. Nekrasov, ed., Stroizdat, Moscow, 32–45.
- Zi, G., and Bažant, Z. P. (2001). "Continuous relaxation spectrum for concrete creep and its incorporation into microplane model M4." *J. Eng. Mech.*, 128(12), 1331–1336.
- Zi, G., and Bažant, Z. P. (2003). "Decontamination of radionuclides from concrete by microwave heating. II: Computations." *J. Eng. Mech.*, 129(7), 785–792.

# Decontamination of Radionuclides from Concrete by Microwave Heating. II: Computations

Goangseup Zi<sup>1</sup> and Zdeněk P. Bažant, F.ASCE<sup>2</sup>

**Abstract:** Based on a mathematical model developed in the preceding Part I of this study, a numerical analysis of the process of decontamination of radionuclides from concrete by microwave heating is conducted. The aim is to determine the required microwave power and predict whether and when the contaminated surface layer of concrete spalls off. As customary, the finite element method is used for the stress and fracture analysis. However, as a departure from previous studies, the finite volume method is adopted to treat the heat and moisture transfer, in order to prevent spurious numerical oscillations that plagued the finite element response at moving sharp interface between the saturated and unsaturated concrete, and to deal accurately with the jumps in permeability and in sorption isotherm slope across the interface. The effects of wall thickness, reinforcing bars, microwave frequency, and power are studied numerically. As a byproduct of this analysis, the mechanism of spalling of rapidly heated concrete is clarified.

**DOI:** 10.1061/(ASCE)0733-9399(2003)129:7(785)

**CE Database subject headings:** Computation; Concrete; Microwaves; Contamination; Contaminants; Heating; Diffusion; Thermal stresses; Pore pressure.

## Introduction

Based on the model developed in the preceding Part I of this study (Bažant and Zi 2003), we will now conduct numerical analysis of the evolution of the fields of temperature, pore pressure, and stress during rapid microwave heating and analyze the implications for the process of radionuclide decontamination of concrete. For stress and deformation analysis, we will employ the finite element method [Fig. 1(b)]. On the other hand, for the heat and moisture transfer, we will adopt the finite volume method [Fig. 1(a)], which will be a departure from the previous practice in nuclear reactor safety research and fire research (Bažant and Thonguthai 1978, 1979; Bažant and Kaplan 1996; Ahmed and Hurst 1997). Thanks to enforcing exactly the local mass and heat conservation even though the water and heat fluxes are only approximate, this method (Patankar 1980) can suppress the spurious numerical oscillations that have previously been experienced with finite elements in rapid heating problems characterized by a sharp moving interface between saturated and unsaturated regions, associated with jumps in permeability and sorption isotherm slope across the interface (Bažant and Thonguthai 1978, 1979; Celia et al. 1990). For discretization in time, we will employ Picard's method, in which the differential equation coefficients are kept constant during each iteration process, in order to cope with the

severe nonlinearity of the model. The analysis by finite volume method will be simplified as axisymmetric, which is doubtless an adequate approximation.

The material subroutine for the nonlinear triaxial stress-strain relation with strain-softening will be based on microplane model M4 recently developed at Northwestern University. The strains will be assumed to be small. To avoid using too small time steps because of numerical stability problems, we will use an implicit rather than explicit finite element formulation. On the other hand, since the calculation of the tangential stiffness matrix of the microplane model M4 is quite computationally demanding, the initial stiffness matrix will be used in an iterative solution of the system of nonlinear equilibrium equations.

## Effects of Power Pattern

The power of the electromagnetic field produced by a point source placed in a free space (having no dielectric loss) decays in space in proportion to  $r^{-2}$ , where  $r$  = distance between the source and a point where the power is measured. This decay is reflected in the Poynting vector (e.g., Cheng 1983). The power decay in space is affected by the composition of the medium, the type of antenna and other factors.

The effects of various power patterns must be solved from the Maxwell equations [see Eqs. (2a) and (2b) in Part I]. Both the applicator (antenna) (Fig. 1 in Part I) and concrete need, in general, to be included in the analysis of electromagnetic wave propagation. The power may be approximately considered to flow within a cone (called the solid angle) of a certain constant slope  $k$  (Kraus 1988). The effective power flux reduction due to the spreading of the cross section of this cone with distance  $s$  from the applicator may be approximated by the ratio

$$f(x) = y_0^2 / (y_0 + kx)^2 \quad (1)$$

where  $y_0$  = equivalent radius of the applicator at  $x=0$ . Taking  $y_0 = 6$  cm and  $k \approx 0.5$ , one finds the power reduction due to cross

<sup>1</sup>Research Associate, Dept. of Civil Engineering, Northwestern Univ., 2145 Sheridan Rd., Evanston, IL 60208. E-mail: g-zi@northwestern.edu

<sup>2</sup>McCormick School Professor and W. P. Murphy Professor of Civil Engineering and Materials Science, Northwestern Univ., 2145 Sheridan Rd., Evanston, IL 60208. E-mail: z-bazant@northwestern.edu

Note. Associate Editor: Franz-Josef Ulm. Discussion open until December 1, 2003. Separate discussions must be submitted for individual papers. To extend the closing date by one month, a written request must be filed with the ASCE Managing Editor. The manuscript for this paper was submitted for review and possible publication on March 12, 2002; approved on October 29, 2002. This paper is part of the *Journal of Engineering Mechanics*, Vol. 129, No. 7, July 1, 2003. ©ASCE, ISSN 0733-9399/2003/7-785-792/\$18.00.

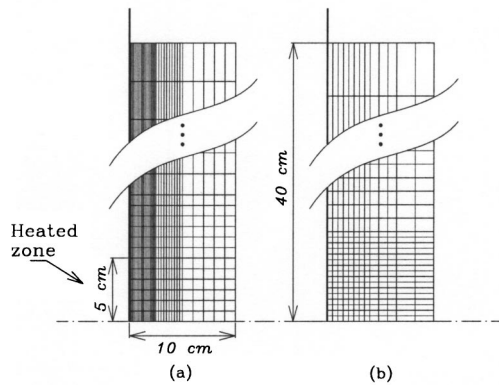


**Fig. 1.** (a) Finite volume mesh for analysis of heat and moisture transfer and (b) finite element mesh for analysis of mechanical deformation in which the size of one element of heated zone is set to 5 mm

section spreading to be about  $f(x) = 90\%$  at  $x = 2$  cm. But at that distance the heat generation rate for  $f = 18.0$  GHz is reduced to almost zero (Fig. 2). Therefore, the spreading of the effective cross section of the power flux can be neglected in practice.

### Applicator Efficiency

A more important aspect of the decontamination process is the efficiency of the applicator. Obviously, the maximum efficiency is obtained for surface reflection coefficient  $R_0 = 0$  [Eq. (5) in Part I], which means that 100% of the power input gets transmitted from the applicator into the concrete. In that case, the intrinsic impedance of the applicator,  $\eta_a$ , is equal to that at concrete surface,  $\eta_1$ . Introducing an empirical efficiency parameter  $\phi \in [0, 1]$ , one may write

$$\eta_a = \phi \eta_1 + (1 - \phi) \eta_0 \quad (2)$$

where  $\eta_0$  = intrinsic impedance of air. Here it is assumed that the intrinsic impedance of the applicator is in the range of  $[\eta_0, \eta_1]$ . The heat generation rates with the maximum efficiency (i.e.,  $\eta_a = \eta_1$ ) are plotted in Fig. 2(b) for different frequencies. For frequency  $f = 18.0$  GHz, the surface heat generation rate is almost

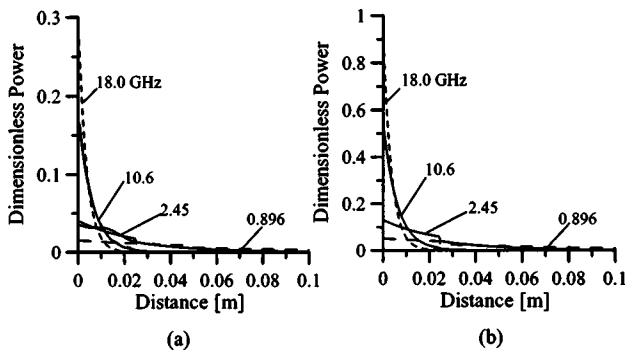


**Fig. 2.** Examples of volumetric heat generations calculated by Eq. (12) in Part I; (a) with zero applicator efficiency, in which heat generations for  $f = 2.45, 10.6$  GHz are compared to heat generations averaged only in time, Eq. (11) in Part I; (b) with maximum efficiency; here, reinforcing bars are located 2.5 cm under surface to which transmission electron microscopy waves are incident

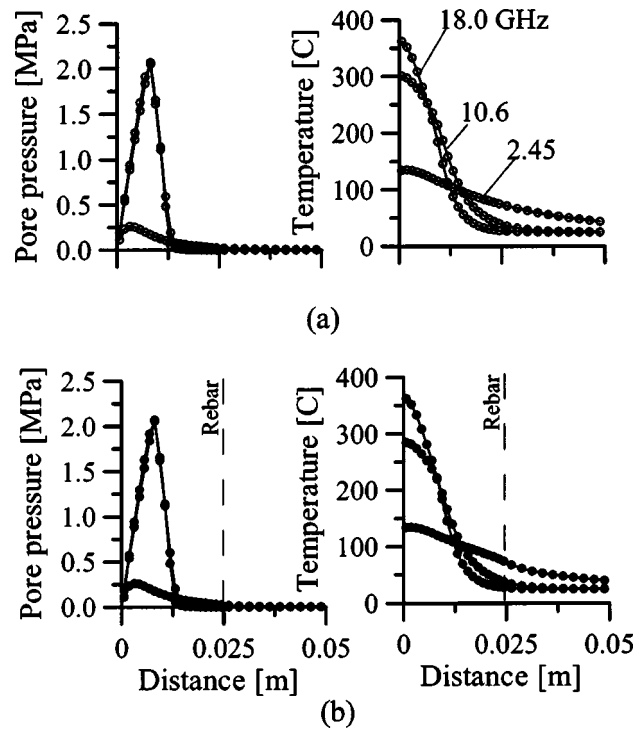


**Fig. 3.** Effect of reinforcing bars in 10 cm wall where 19% of reinforcing bars are located in 2.5 cm from heating surface: (a) without reinforcing bars (circles) and (b) with reinforcing bars (solid dots)

three times higher than that without any optimization [i.e.,  $\eta_a = \eta_0$ ; Fig. 2(a)]. It thus becomes clear that the efficiency  $\phi$  of the applicator is a very important parameter, overwhelming others. Since the efficiency has not been measured experimentally,  $\phi = 50\%$  is assumed for the studies that follow.

### Validity of Spatial Averaging of Heat Generation

The simple heat generation in Eq. (12) in Part I is obtained by means of the temporal and spatial averaging of the ohmic heat dissipation of Eq. (1) in Part I. The heat generation by temporal and spatial averaging [Eq. (12) in Part I] is compared to the heat generation by temporal averaging [Eq. (11) in Part I] in Fig. 2(a) for two frequencies:  $f = 2.45$  and  $10.6$  GHz. The former is a smooth exponential function while the latter oscillates along the radiation direction. However, the difference is negligible for  $f = 2.45$  and visually indistinguishable for  $f = 10.6$  GHz. This shows that the averaging over both space and time is justified for the practical frequency range.

### Effect of Reinforcing Bars on Pore Pressures and Temperatures

As mentioned in Part I (Bažant and Zi 2003), the power carried by microwaves gets reflected from conductive materials, such as the steel reinforcing bars. To investigate this effect, the temperature and pore pressure profiles after 10 s of heating that are obtained in the absence of steel bars [Fig. 3(a)] are compared to the profiles with reinforcing bars [Fig. 3(b)] for three different microwave frequencies,  $f = 2.45, 10.6,$  and  $18.0$  GHz, after 10 s of heating. The area fraction of the steel bars (in a projection on the

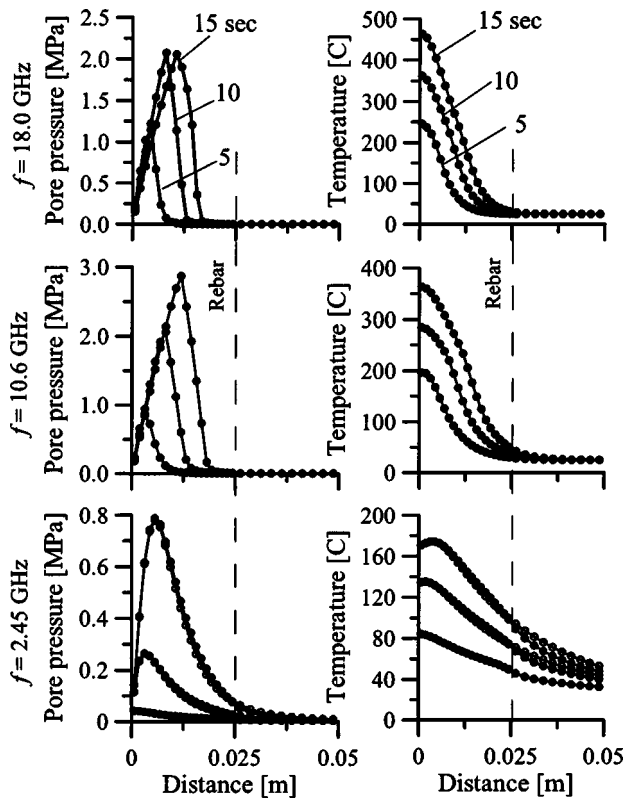


**Fig. 4.** Effect of different frequencies on pore pressure and temperature profiles; solid dots represent the case with reinforcing bars and circles represent the case without reinforcing bars

surface of the wall) is considered to be about 19%. The location of the bars is marked by the dashed lines in the figure.

The center of the reinforcing bars in concrete structures is located typically at 2.5–4 cm below the surface. At that depth, the electromagnetic power is almost exhausted by the power dissipation (Fig. 2). Therefore, it appears that the existence of steel bars is not important for the decontamination process. However, note that this argument is not true in general. It holds true only for the high-power decontamination process and typical reinforced concrete structures. If much lower frequencies were used or if a conductive material, the steel, were located closer to the concrete surface, this effect could get important.

### Effect of Microwave Frequencies on Pore Pressures and Temperatures

The effects of different frequencies,  $f = 2.45, 10.6,$  and  $18.0$  GHz, are plotted in Fig. 4. The same initial power density,  $P_0 = 1.1 \text{ MW/m}^2$ , is considered for every case. As the frequency increases, the location of the peaks of pore pressure and temperature shift toward the heated surface. The reason is that the energy dissipation rate is higher at a higher frequency.

The maximum pore pressure for  $f = 18.0$  GHz after 10 seconds of heating is  $P_{\max,10} = 2.0 \text{ MPa}$  at 7.5 mm below the surface. If this pore pressure acted on an unrestrained element of concrete, it would produce in concrete the tensile volumetric (hydrostatic) stress  $\sigma_v \approx 0.1 \times 2.0 = 0.2 \text{ MPa}$ , where the value 0.1 is adopted for the typical porosity of concrete. Compared to the tensile strength of ordinary concrete,  $f'_t \approx 4 \text{ MPa}$ , this value of tensile volumetric stress is only about 5% of  $f'_t$ .

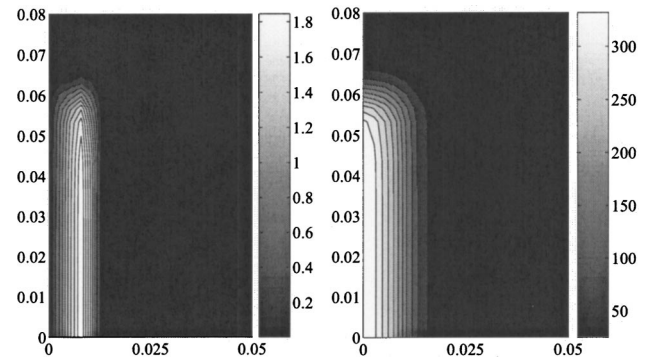


**Fig. 5.** Contour plot of development of pore pressure (left; MPa) and temperature (right; °C) after 10 heating with  $f = 18.0$  GHz and  $P_0 = 1.1 \text{ MW/m}^2$

The effect of pore pressure is in fact even weaker since the foregoing estimate is the maximum possible pore pressure if the additional pore space created by the formation of microcracks has been neglected. Taking it into account, an even smaller tensile volumetric stress in an unrestrained element of concrete would be indicated. So, although the effect of pore pressure is not completely negligible, it cannot be the main cause of spalling.

Fig. 5 shows the contour plot of pore pressure and temperature that develops after 10 s of heating at frequency  $f = 18.0$  GHz and power input  $P_0 = 1.1 \text{ MW/m}^2$ . As we can see, the heated zone is localized very near the heated surface.

### Stress Fields and Triggering of Spalling

Because the distributed cracking described by the microplane model represents strain softening, the stress and deformation analysis must employ some localization limiter (Bažant 2002), which could have the form of either the crack band model or some of the nonlocal models (Bažant and Ožbolt 1990, 1992; Ožbolt and Bažant 1996; Jirásek and Bažant 2002). The former has been adopted for the present purpose. Thus the finite element size  $l_c$  is fixed as a material property. The proper value of  $l_c$  depends on the postpeak softening slope of the uniaxial tensile response given by the constitutive model.

The constitutive model gives a good match of material test data when the finite element in the test specimens size is about 5 mm. The same finite element size  $l_c$  is, therefore, adopted here, although this is less than the typical maximum aggregate size in concrete. The thickness of the layer that spalls off within about 10 seconds as a result of microwave heating is also about 5 mm, as revealed by experimental trials of microwave induced spalling (White et al. 1995). Unfortunately, the data from these trials cannot be used to verify the present theoretical predictions because the material properties were not documented (not even the compressive strength  $f'_c$  of the concrete in the wall subjected to microwave heating was measured). Only the average depth of the removed surface layer was recorded (White et al. 1995). Therefore, the typical properties of concrete used in the nuclear facilities had to be assumed for the present numerical simulations.

Fig. 6 shows the available experimental data (Jansen and Shah 1997) and their numerical fitting using the present theoretical model. Fig. 7 depicts the constant-value contour plots of the computed strain field after 10 s of microwave heating; it shows the mechanical strain, i.e., the total (elastic plus viscoelastic) strain

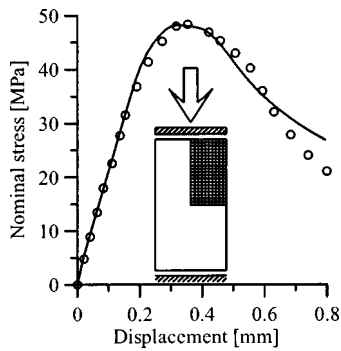


**Fig. 6.** Uniaxial compression data of 10.17 cm×20.03 cm cylinder tested by Jansen and Shah (1997) (circles) and its optimal fitting (solid line) by finite element simulation in which axisymmetric quadrilateral elements of size 5 mm by 5 mm are used;  $E=48.5$  GPa,  $k_1=0.000125$ ,  $k_2=160.0$ ,  $k_3=6.4$ , and  $k_4=150.0$

minus the hygrothermal strain (strain produced by changes of temperature and water content). It is found that the maximum principal mechanical strain in the surface layer exceeds 0.005 in tension and the strain state is essentially biaxial (Fig. 8). This strain value is much higher than the typical strain at peak in uniaxial tension (about 0.0002). It follows that the concrete must undergo postpeak softening and suffer disintegration by cracking. The compressive stress induced by the temperature increase is resisted not only by radial and circumferential biaxial compression generated by the resistance of the cold concrete mass surrounding the heated zone, but also by tensile stress in the circumferential direction of the axisymmetric mesh caused by radial expansion (a situation similar to that analyzed by Ulm et al., 1999).

### Is Spalling Triggered by Pore Pressure or Compressive Thermal Stress?

The question of the main cause of spalling of the surface layer of a rapidly heated concrete wall has been the subject of many debates. One school of thought, initiated by Harmathy (1965, 1970), Harmathy and Allen (1973), Li et al. (1993), and Lagos et al. (1995), holds that the pore water cannot escape fast enough (a phenomenon called “moisture clog”) and thus develops high vapor pressures which cannot be resisted by the tensile strength of

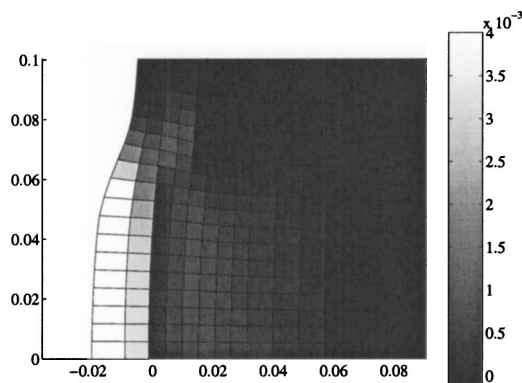


**Fig. 7.** Contour plot of mechanical strain  $\epsilon_1$  after 10 s heating, in which deformation is exaggerated by 100

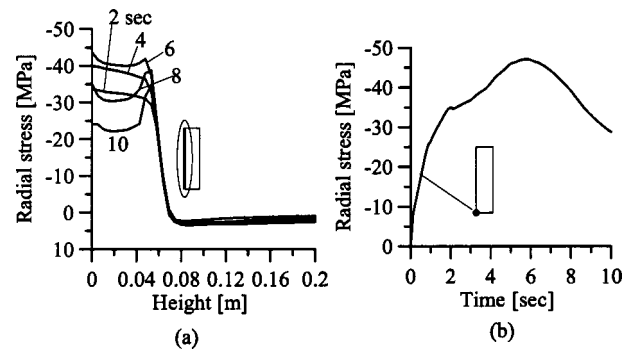


**Fig. 8.** (a) Distribution of radial stress with respect to height and (b) evolution of radial stress at center of heated zone by time

concrete. Another school of thought (Bažant 1997) is that the thermal expansion of the saturated heated zone, resisted by the cold concrete mass that surrounds the heating zone, leads in the surface layer to very high compressive stresses parallel to surface which either crush concrete, or cause the compressed surface layer to buckle, or both.

The relative significance of these two mechanisms must of course depend on the type of problem, and can be different for microwave heating in the bulk of concrete and for conductive heating by fire. In the present problem, the highest pore pressure calculated has the value 2.0 MPa, which causes in concrete a hydrostatic tension of about 0.2 MPa. This value is not enough to initiate spalling concrete. Besides, as soon as cracks start to form, the volume available to pore water rapidly increases (by orders of magnitude), which must cause a rapid drop of pore pressure before the cracks can become large and open widely (Bažant 1997).

So it appears that the pore pressure development cannot be the main cause of spalling, although it is not a negligible factor in the triggering of spalling. The main cause must be the compressive stresses along radial lines emanating from the center of the heated zone. These stresses, engendered by the resistance of cold concrete to the thermal expansion of the heated zone, reach values as high as about 50 MPa [Fig. 8(b)], according to the present analysis. This is certainly enough to cause compressive crushing as well as buckling of the compressed layer.

### Application of Finite Volume Method to Heat and Water Transfer in Concrete

Since the finite volume method (Eymard et al. 1998, 2000) has not been used for the coupled heat and water transfer problems of concrete, its application will now be described. In this method, the domain is divided into discrete control volumes (Fig. 9). The interfaces (or boundaries) of a control volume are placed midway between adjacent representative points (which is generally accomplished by Voronoi tessellation, although that approach is not needed for the regular node arrangement used here). The discretization equations are derived by integrating Eqs. (19) and (20) of Part I over the control volume shown in Fig. 9(a), and over the time interval from  $t$  to  $t + \Delta t$

$$\begin{aligned} & (w_0^{i+1,m+1} - w_0^i) + c_x(J_e - J_w)^{i+1,m+1} + c_y(J_n - J_s)^{i+1,m+1} \\ & = I_{(w)}^{i+1,m+1} \end{aligned} \quad (3)$$

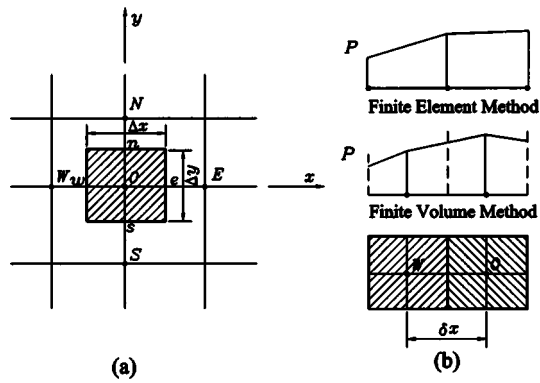


**Fig. 9.** (a) Two dimensional discretization of finite volume where  $W, E, S, N$  = labels for West, East, South, and North; shaded rectangle represents control volume and (b) difference in pressure (or temperature) profiles implied by finite element and finite volume methods

$$[(\rho C)_0(T_0^{i+1,m+1} - T_0^i)] + c_x(q_e - q_w)^{i+1,m+1} + c_y(q_n - q_s)^{i+1,m+1} = I_{(h)}^{i+1,m+1} \quad (4)$$

where  $i$  = label for time step ( $i = 1, 2, \dots$ );  $m$  = label for iteration number in an implicit scheme ( $m = 1, 2, \dots$ );  $0$  = label for current control volume [the center point in Fig. 9(a)];  $s, e, n, w$  = labels for south, east, north, and west interfaces, respectively, of a square control volume in Fig. 9;  $c_x = \Delta t / \Delta x$  and  $c_y = \Delta t / \Delta y$  for a two-dimensional plane flow problem;  $c_y = \Delta t / y_0 \Delta x$  if  $y$  is the radial direction in the axisymmetric flow problem, where  $y_0$  is the radial distance of point  $0$  from the radial center; and  $\Delta x, \Delta y$  = sizes of the current control volume (Fig. 9). Due to severe nonlinearity of the problem, modified Picard's iteration (Celia et al. 1990), in which the differential coefficients of the fluxes are taken as constants during each iteration, is adopted to solve the partial differential equations.

To calculate the fluxes at the control-volume interfaces, linear distributions of the state variables between the representative points are assumed. This simplifies the calculation of the flux at an interface. For example,

$$J_w = -\frac{a_w}{g} \frac{P_0 - P_w}{x_0 - x_w} \quad (5)$$

where  $J_w$  = water flux through the interface  $W$  (west);  $a_w$  = interface permeability at interface  $W$ ;  $P_0, P_w$  = pore pressures at points  $0$  and  $W$  (west); and  $x_0, x_w$  = distances of the points  $0$  and  $W$  from the center [Fig. 9(a)].

Note that, in the finite volume method, the flux  $J_w$  at the west interface of current control volume  $0$  [Fig. 9(b)] is exactly equal to the flux  $J_e$  at the east interface of the adjacent control volume lying to the west, even though the flux values are only approximate. Therefore, the condition of local mass balance (as well the condition of local heat balance) is satisfied in the finite volume method exactly. This is a well-known advantage of the finite volume method, important for avoiding spurious oscillation in highly nonlinear problems with high local gradients and sharp fronts. The advantage of the finite volume method for the analysis of moisture transfer in concrete was recognized already by Eymard et al. (1998) and was explored by Mainguy and Coussy (2000) in the problem of calcium leaching from concrete, although in the absence of heat transfer. Mainguy et al. (2001a) showed an effective application of the finite volume method to drying of porous materials.

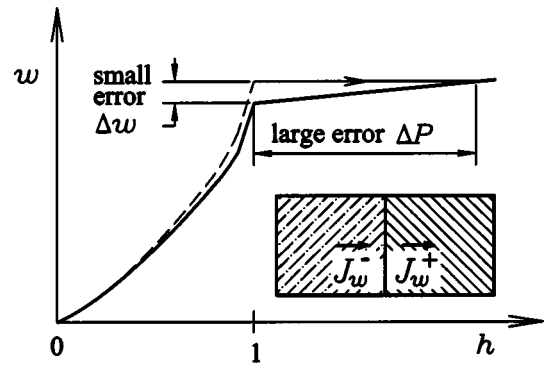


**Fig. 10.** Explanation why small error in water content caused by lack of exact mass balance can cause enormous error in pore pressure

In the finite element approach, by contrast, the local mass balance cannot be satisfied exactly. For example, if standard finite elements with linear shape functions are used [Fig. 9(b)], then the flux at the west boundary of the current control volume is generally different from the flux at the east boundary of the adjacent control volume lying to the west [note the different slopes adjoining the interface in Fig. 9(b)]. Nevertheless, for a special case of mass lumping (achieving pressure interpolation imitating the finite volume method), in low-order finite elements and for implicit time integration applied to coupled diffusion-dissolution problems, the finite element method gives the same results as the finite volume method and provides an accurate oscillation-free determination of sharp fronts (Mainguy et al. 2001b).

The reason why exact local mass balance is needed to avoid spurious oscillation of pressure and concentration (water content) is explained by Fig. 10, showing a sharp change of slope of the sorption isotherm of relative pore pressure  $h$  (humidity) versus water concentration  $w$  (specific pore water content). At the transition from unsaturated to saturated state ( $h=1$ ), a very small error  $\Delta w$  in water concentration, which is insignificant for the pressures in the unsaturated states, is seen to cause an enormous change of pressure in the saturated state (because the slope of the pressure concentration isotherm drops above  $h=1$  by orders of magnitude). This means that if the control volume with outflux  $J_w^-$  is unsaturated and the adjacent control volume with influx  $J_w^+$  is saturated, even a very small error in  $J_w^-$  would cause a very large pressure change in the saturated control volume.

The heat generation  $I_{(h)}$  depends on the water contents of all the control volumes along the wave propagation path. The water contents, in turn, depend on the pore pressures and temperatures produced by the microwave heating. To avoid the complication that stems from this mutual coupling, the heat generation  $I_{(h)}$  is in each time step calculated explicitly, based on the water contents of the control volumes in the last previous time step. The error caused by this one-step delay in the calculation of heat generation is very small if a small time step is used.

After taking the first-order Taylor expansion of the terms superscripted by  $m+1$  and collecting the terms that contain the variations  $\delta P$  and  $\delta T$  from one iteration to the next (in the same time step), one obtains the following system of algebraic linear equations:

$$K_{P_0}^M \delta P_0 + K_{P_w}^M \delta P_w + K_{P_s}^M \delta P_s + K_{P_e}^M \delta P_e + K_{P_n}^M \delta P_n + K_{T_0}^M \delta T_0 + K_{T_w}^M \delta T_w + K_{T_s}^M \delta T_s + K_{T_e}^M \delta T_e + K_{T_n}^M \delta T_n = R^M \quad (6)$$

$$K_{P_0}^H \delta P_0 + K_{P_W}^H \delta P_W + K_{P_S}^H \delta P_S + K_{P_E}^H \delta P_E + K_{P_N}^H \delta P_N + K_{T_0}^H \delta T_0 + K_{T_W}^H \delta T_W + K_{T_S}^H \delta T_S + K_{T_E}^H \delta T_E + K_{T_N}^H \delta T_N = R^H \quad (7)$$

where

$$K_{P_0}^M = c_x(a_w^{i+1,m}/\delta x_w) + c_y(a_s^{i+1,m}/\delta x_s) + c_x(a_e^{i+1,m}/\delta x_e) + c_y(a_n^{i+1,m}/\delta x_n) \quad (8)$$

$$K_{P_W}^M = -c_x(a_w^{i+1,m}/\delta x_w), \quad K_{P_S}^M = -c_y(a_s^{i+1,m}/\delta x_s), \quad (9)$$

$$K_{P_E}^M = -c_x(a_e^{i+1,m}/\delta x_e), \quad K_{P_N}^M = -c_y(a_n^{i+1,m}/\delta x_n) \quad (10)$$

$$K_{T_0}^M = (\partial w/\partial T)^{i+1,m} - (\partial I_{(w)}/\partial T)^{i+1,m}, \quad K_{T_W}^M = K_{T_S}^M = K_{T_E}^M = K_{T_N}^M = 0 \quad (11)$$

$$R^M = -[(w_0^{i+1,m} - w_0^i) + c_x(J_e - J_w)^{i+1,m} + c_y(J_n - J_s)^{i+1,m} - I_{(w)}^{i+1,m}] \quad (12)$$

$$K_{P_0}^H = K_{P_W}^H = K_{P_S}^H = K_{P_E}^H = K_{P_N}^H = 0 \quad (13)$$

$$K_{T_0}^H = \rho C \quad (14)$$

$$K_{T_W}^H = -c_x(k_w^{i+1,m}/\delta x_w), \quad K_{T_S}^H = -c_y(k_s^{i+1,m}/\delta x_s), \quad (15)$$

$$K_{T_E}^H = -c_x(k_e^{i+1,m}/\delta x_e), \quad K_{T_N}^H = -c_y(k_n^{i+1,m}/\delta x_n) \quad (16)$$

$$R^H = -[\rho C T^{i+1,m} + c_x(q_e - q_w)^{i+1,m} + c_y(q_n - q_s)^{i+1,m} - I_{(h)}] \quad (17)$$

Here  $\delta x$ ,  $\delta y$  = distances between the representative points of adjacent control volumes [Fig. 9(b)];  $M$  = label for mass;  $H$  = label for heat;  $R$  = residual which is to be reduced to almost zero by the iteration;  $S, E, N, W$  = labels for control volumes adjacent to the current control volume 0 in the direction of south, east, north, and west, respectively, in Fig. 9(a);  $a$  = interface permeability; and  $k$  = interface heat conductivity.

The differential coefficients of the fluxes need to be multiplied by the radial distance of the corresponding interfaces if an axisymmetric problem is considered. The interface permeability is easily computed from the mass conservation condition. For example, if a steady state flow is considered, the mass flux on the interface  $w$  measured with respect to west control volume must be equal to the mass flux measured with respect to the current control volume 0 [see Fig. 9(a)]. Therefore, the equivalent permeability of the interface is

$$a_w = \frac{a_w a_0}{f a_w + (1-f) a_0} \quad (18)$$

where  $f$  = constant representing the location of interface;  $a_w$  = representative permeability of west control volume; and  $a_0$  = representative permeability of current control volume. The interface heat conductivity is calculated by Eq. (18) similarly. One can calculate the interface permeability at boundaries from Eq.

(18), too. For example, when the surface emissivity is infinite, the interface permeability of the west boundary surface is  $a = a_0$ .

## Conclusions

1. The computations confirm that the power and efficiency of the microwave applicator is a key factor for the proposed decontamination process. For the maximum power efficiency considered, the heat generation per unit volume of the wall is almost three times greater than it is for zero efficiency. Therefore the efficiency should be accurately measured.
2. In view of the high microwave frequencies considered, averaging of the heating rate over the spatial wavelength and the time period causes no appreciable error.
3. The calculations confirm that a 5 mm thick surface layer of typical concrete can be spalled off within 10 s of microwave heating of frequency 18.0 GHz and power 1.1 MW/m<sup>2</sup>.
4. Calculations show that the thickness of the concrete wall has a negligible effect on the evolution of pore pressure and temperature. The reason is the short heating duration which is of the order of 10 s only. For long heating durations, differences would of course be obtained, due to microwave reflection and heat loss at the opposite surface of wall.
5. The electromagnetic power carried by the microwaves is almost exhausted when the waves reach the location of the reinforcing bars in typical concrete structures. Therefore, the same decontamination process can be used for both unreinforced and reinforced concrete walls.
6. The pore water pressure caused by heating is not negligible but is not a major factor. The main cause of spalling is high compressive stress parallel to surface along the radial lines emanating from the heated zone and high tensile stress along the circumferential lines, both produced by thermal expansion of the heated zone confined by cold concrete.
7. The present computational experience confirms that the finite volume method is preferable to the finite element method for simultaneous heat and mass transfer in concrete heated to high temperature. Adoption of this method helps to eliminate spurious oscillations of response caused by propagation of a sharp interface with order-of-magnitude jumps in pore pressure and permeability (the interface separates a saturated zone from a nonsaturated zone, or a cold zone of small permeability from a hot zone of a high permeability).

## Acknowledgments

Grateful appreciation is due to the Department of Energy for supporting both parts of this study under Grant No. DE-FG07-98ER45736 to Northwestern University. Thanks are due to Dr. Brian Spalding of the Oak Ridge National Laboratory for valuable consultations and constructive monitoring of the progress of this research.

## Appendix I: Input Data for Analysis

The input data for the parametric studies of microwave heating in Figs. 3, 4, 5, and 11 are as follows: age of concrete = 20 years; initial relative humidity in the pores  $h_0 = 0.6$ ;  $T_0 = 25.0^\circ\text{C}$ ; saturation water content = 135 kg/m<sup>3</sup>; apparent mass density of concrete = 2288 kg/m<sup>3</sup>; heat capacity of concrete = 1000 J/kg °K; reference permeability =  $40.5 \times 10^{-12}$  m/s; heat conductivity

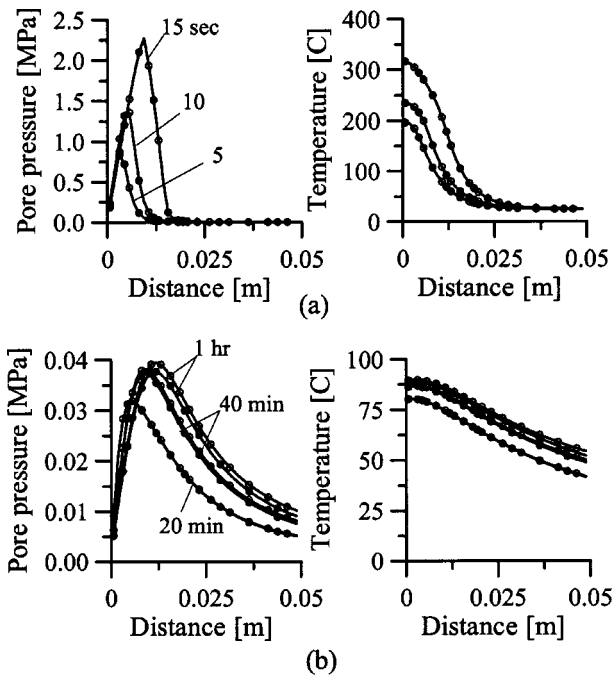


**Fig. 11.** Effect of wall thickness on pore pressure and temperature profiles in which  $f = 10.6$  GHz is used; (top) rapid heating with high power ( $1.1 \text{ MW/m}^2$ ); (bottom) slow heating with low power ( $0.01 \text{ MW/m}^2$ ). Solid dots represent profiles across 30 cm wall and circles represent profiles across 10 cm wall.

$= 3.67 \text{ J/m}^2 \text{ s } ^\circ\text{C}$ ; amount of unhydrous cement  $= 227 \text{ kg/m}^3$ ; mass transfer coefficient of water flux  $= \infty$ ; heat transfer coefficient of heat flux  $= 10.0 \text{ J/m}^2 \text{ s } ^\circ\text{C}$ ; relative dielectric permittivity  $\epsilon'/\epsilon_0$  of concrete  $= 5.0$ ; surface emissivity  $= 0.9$ ; the range of frequencies applied  $= 2.45\text{--}18.0$  GHz; the initial power density  $= 1.1 \text{ MW/m}^2$  for the rapid heating and  $0.011 \text{ MW/m}^2$  for the slow heating; the area fraction of reinforcing bars in a plane parallel to surface  $= 19\%$ ; distance of the centroid of reinforcing bars from concrete surface  $=$  at least 2.5 cm.

The input data for the mechanical deformation analysis are:  $E = 48.5 \text{ GPa}$ ;  $k_1 = 0.000125$ ,  $k_2 = 160$ ,  $k_3 = 6.4$ , and  $k_4 = 150.0$  for the microplane model; the thermal expansion coefficient  $= \alpha_T = 12.0 \times 10^{-6}$ .

## Appendix II: Effect of Wall Thickness on Pore Pressures and Temperatures

Fig. 11(a) shows the pore pressure and temperature profiles for two different wall thicknesses, 10 and 30 cm, after 5, 10, and 15 s of heating with the power density  $P_0 = 1.1 \text{ MW/m}^2$ , which is quite high and equals the power intensity used by White et al. (1995). For the short durations (about 10 s), contemplated for the decontamination process, the profiles obtained for two different wall thicknesses are almost identical (White et al. 1995) (and doubtless also about the same as in a half space).

If the wall were heated for a relatively long time with a low power density, appreciable differences in the temperature profiles would be observed because of the power reflected from the wall surface opposite to the heated surface; see Fig. 11(b);  $P_0 = 0.01 \text{ MW/m}^2$ . A wall 10 cm thick would be heated a little faster than a wall 30 cm thick. But the differences are still very small.

## Appendix III: Review of Microplane Constitutive Model for Concrete

For readers's convenience, model M4, already mentioned and referenced to in Part I will now be summarized (Bažant et al. 2000; Caner and Bažant 2000). The strain vectors on the plane of any orientation within the material, called the microplane, are assumed to be the projections of the continuum (macroscopic) strain tensor  $\epsilon_{ij}$  (where the subscripts,  $i, j = 1, 2, 3$  refer to Cartesian coordinates  $x_i$ ). This is called the kinematic constraint. Thus the component of the strain vector  $\epsilon_j^n$  on any microplane is  $\epsilon_j^n = \epsilon_{jk} n_k$  (Bažant and Prat 1988) where  $n_i$  are the direction cosines of the normal to the microplane. The normal strain vector is  $\epsilon_{N_i} = n_i n_j n_k \epsilon_{jk}$ , and its magnitude is  $\epsilon_N = n_j \epsilon_j^n = n_j n_k \epsilon_{jk} = N_{ij} \epsilon_{ij}$ , where  $N_{ij} = n_i n_j$  (the repeated Latin lowercase subscripts indicate summation over 1, 2, 3). The magnitude of the strain vector on the microplane is  $\|\epsilon_j^n\| = \sqrt{\epsilon_j^n \epsilon_j^n}$ . The shear strain components in two orthogonal (suitably chosen) directions  $m_i$  and  $l_i$  tangential to the microplane (normal to  $n_i$ ) are  $\epsilon_M = m_i (\epsilon_{ij} n_j)$  and  $\epsilon_L = l_i (\epsilon_{ij} n_j)$ . Because of the symmetry of  $\epsilon_{ij}$ ,  $\epsilon_M = M_{ij} \epsilon_{ij}$ ,  $\epsilon_L = L_{ij} \epsilon_{ij}$ , where  $M_{ij} = (m_i n_j + m_j n_i)/2$  and  $L_{ij} = (l_i n_j + l_j n_i)/2$  (Bažant and Prat 1988).

Since the kinematic constraint relates the strains on the microplanes to the macroscopic strain tensor, the static equivalence can be enforced only approximately. This is done by means of the virtual work theorem which is written for the surface of a unit hemisphere (Bažant 1984)

$$\frac{2\pi}{3} \sigma_{ij} \delta \epsilon_{ij} = \int_{\Omega} (\sigma_N \delta \epsilon_N + \sigma_L \delta \epsilon_L + \sigma_M \delta \epsilon_M) d\Omega \quad (19)$$

$$= \int_{\Omega} (\sigma_N N_{ij} + \sigma_L L_{ij} + \sigma_M M_{ij}) \delta \epsilon_{ij} d\Omega \quad (20)$$

The normal stress and normal strain are split into their volumetric and deviatoric parts, and if Eq. (20) is written separately for the volumetric and deviatoric components, one has

$$\sigma_{ij} = \sigma_V \delta_{ij} + \sigma_D^D \quad (21)$$

$$\sigma_D^D = \frac{3}{2\pi} \int_{\Omega} \left[ \sigma_D \left( N_{ij} - \frac{\delta_{ij}}{3} \right) + \sigma_L L_{ij} + \sigma_M M_{ij} \right] d\Omega \quad (22)$$

The elastic increments of the stresses in each microplane over the time step (or load step) are written as  $\Delta \sigma_V = E_V \Delta \epsilon_V$ ,  $\Delta \sigma_D = E_D \Delta \epsilon_D$ , and  $\Delta \sigma_T = E_T \Delta \epsilon_T$ , where  $E_V = E/(1 - 2\nu)$ ;  $E_D = 5E/(2 + 3\eta)(1 + \nu)$ , and  $E_T = \eta E_D$ . Here  $\eta$  is a parameter that can be chosen; the best choice is  $\eta = 1$  (Carol et al. 1991; Bažant et al. 1996; Carol and Bažant 1997). The volumetric–deviatoric split makes it possible to reproduce the full range of Poisson ratio  $-1 \leq \nu \leq 0.5$  in elastic analysis. The term  $-\delta_{ij}/3$  in Eq. (22) ensures that  $\sigma_{kk}^D = 0$  even when  $\int_{\Omega} \sigma_D d\Omega \neq 0$ .

The integration is conducted numerically according to an optimal Gaussian quadrature integration formula for a spherical surface, characterized by discrete directions  $\mu$  and associated weights  $w_\mu$ ;  $\sigma_{ij} = (3/2\pi) s_{ij} \approx 6 \sum_{\mu=1}^N w_\mu s_{ij}^{(\mu)}$ , where  $s_{ij} = \int_{\Omega} (\sigma_N N_{ij} + \sigma_L L_{ij} + \sigma_M M_{ij}) \delta \epsilon_{ij} d\Omega$  and  $N$  is the number of the microplanes.

The inelastic behavior with fracturing damage, modeled as strain softening, is characterized on the microplanes in terms of strain-dependent yield limits for the components  $\sigma_V$ ,  $\sigma_D$ ,  $\sigma_N$ ,  $\sigma_L$  and  $\sigma_M$ , called the stress–strain boundaries. These boundaries can approximately reflect various physical mechanisms such as frictional slip in a certain direction, progressive growth of micro-

cracks of a certain orientation, axial splitting, lateral spreading under compression, etc.

The constitutive model is explicit. In each time step, and at each integration point of each finite element, the newly calculated strain tensor is supplied as the input to the microplane constitutive subroutine. From this, the subroutine first calculates the strain components on all the discrete microplanes (whose number, from experience, must be at least 21, for acceptable accuracy). From those components, the stresses are calculated first elastically, and if any stress component exceeds the value on the stress-strain boundary for the given strain, the stress value is dropped onto the boundary at constant strain. From the stresses on the microplane, the continuum stress tensor is calculated as the output, which is then used by the finite element program to calculate the nodal forces.

## References

- Ahmed, G. N., and Hurst, J. P. (1997). "Coupled heat and mass transport phenomena in siliceous aggregate concrete slabs subjected to fire." *Fire Mater.*, 21, 161–168.
- Bažant, Z. P. (1984). "Microplane model for strain controlled inelastic behavior." *Mechanics of engineering materials*, C. S. Desai and R. H. Gallagher, eds., Chap. 3, Wiley, London, 45–59.
- Bažant, Z. P. (1997). "Analysis of pore pressure, thermal stress and fracture in rapidly heated concrete." *Proc., Int. Workshop on Fire Performance of High-Strength Concrete*, NIST Special Publication 919, L. T. Phan et al., eds., National Institute of Standards and Technology, Gaithersburg, Md., 155–164.
- Bažant, Z. P. (2002). *Scaling of structural strength*, Hermes-Penton, London.
- Bažant, Z. P., Caner, F. C., Carol, I., Adley, M. D., and Akers, S. A. (2000). "Microplane model M4 for concrete I: Formulation with work-conjugate deviatoric stress." *J. Eng. Mech.*, 126(9), 944–953.
- Bažant, Z. P., and Kaplan, M. F. (1996). *Concrete at high temperatures*, Longman, London.
- Bažant, Z. P., and Ožbolt, J. (1990). "Nonlocal microplane model for fracture, damage and size effect in structures." *J. Eng. Mech.*, 116(11), 2484–2504.
- Bažant, Z. P., and Ožbolt, J. (1992). "Compression failure of quasi-brittle material: Nonlocal microplane model." *J. Eng. Mech.*, 118(3), 540–556.
- Bažant, Z. P., and Prat, P. C. (1988). "Microplane model for brittle plastic material: I. Theory." *J. Eng. Mech.*, 114(10), 1672–1688.
- Bažant, Z. P., and Thonguthai, W. (1978). "Pore pressure and drying of concrete at high temperature." *J. Eng. Mech. Div., Am. Soc. Civ. Eng.*, 104(5), 1059–1079.
- Bažant, Z. P., and Thonguthai, W. (1979). "Pore pressure in heated concrete walls: Theoretical prediction." *Mag. Concrete Res.*, 31(107), 67–76.
- Bažant, Z. P., Xiang, Y., and Prat, P. C. (1996). "Microplane model for concrete. I. Stress-strain boundaries and finite strain." *J. Eng. Mech.*, 122(3), 245–254; 123(3), E411–E411.
- Bažant, Z. P., and Zi, G. (2003). "Decontamination of radionuclides from concrete by microwave heating. I: Theory." *J. Eng. Mech.*, 129(7), 777–784.
- Caner, F. C., and Bažant, Z. P. (2000). "Microplane model M4 for concrete II: Algorithm and calibration." *J. Eng. Mech.*, 126(9), 954–961.
- Carol, I., and Bažant, Z. P. (1997). "Damage and plasticity in microplane theory." *Int. J. Solids Struct.*, 34(29), 3807–3835.
- Carol, I., Bažant, Z. P., and Prat, P. C. (1991). "Geometric damage tensor based on microplane model." *J. Eng. Mech.*, 117(10), 2429–2448.
- Celia, M. A., Bouloutas, E. T., and Zarba, R. L. (1990). "A general mass-conservative numerical solution for the unsaturated flow equation." *Water Resour. Res.*, 26(7), 1483–1496.
- Cheng, D. K. (1983). *Field and wave electromagnetics*, Addison-Wesley, London.
- Eymard, R., Gallouët, T., and Herbin, R. (2000). "The fine volume methods." *Handbook of numerical analysis*, P. G. Ciarbet and J. L. Lions, eds., North Holland, Amsterdam.
- Eymard, R., Gallouët, T., Hilhorst, D., and Slimane, Y. N. (1998). "Finite volumes and nonlinear diffusion equations." *RAIRO-Mathematical Modelling and Numerical Analysis—Modélisation Mathématique et Analyse Numérique*, 32(6), 747–761.
- Harmathy, T. Z. (1965). "Effect of moisture on the fire endurance of building materials." *Moisture in Materials in Relation to Fire Tests. ASTM Special Technical Publication No. 385*, American Society of Testing Materials, Philadelphia, 74–95.
- Harmathy, T. Z. (1970). "Thermal properties of concrete at elevated temperatures." *J. Mater.*, 5(1), 47–74.
- Harmathy, T. Z., and Allen, L. W. (1973). "Thermal properties of selected masonry unit concrete." *ACI J.*, 70(2), 132–142.
- Jansen, D. C., and Shah, S. P. (1997). "Effect of length on compressive strain softening of concrete." *J. Eng. Mech.*, 123(1), 25–35.
- Jirásek, M., and Bažant, Z. P. (2002). *Inelastic analysis of structures*, Vol. 735, Wiley, London.
- Kraus, J. D. (1988). *Antennas*, MacGraw-Hill, New York.
- Lagos, L. E., Li, W., and Ebadian, M. A. (1995). "Heat transfer within a concrete slab with a finite microwave heating source." *Int. J. Heat Mass Transf.*, 38(5), 887–897.
- Li, W., Ebadian, M. A., White, T. L., and Grubb, R. G. (1993). "Heat transfer within a concrete slab applying the microwave decontamination process." *J. Heat Transf.*, 115, 42–50.
- Mainguy, M., and Coussy, O. (2000). "Propagation fronts during calcium leaching and chloride penetration." *J. Eng. Mech.*, 126(3), 250–257.
- Mainguy, M., Coussy, O., and Baroghel-Bouny, V. (2001a). "Role of air pressure in drying of weakly permeable materials." *J. Eng. Mech.*, 127(6), 582–592.
- Mainguy, M., Ulm, F.-J., and Heukamp, F. H. (2001b). "Similarity properties of demineralization and degradation of cracked porous materials." *Int. J. Solids Struct.*, 38, 7079–7100.
- Ožbolt, J., and Bažant, Z. P. (1996). "Numerical smeared fracture analysis: Nonlocal microcrack interaction approach." *Int. J. Numer. Methods Eng.*, 39, 635–661.
- Patankar, S. V. (1980). *Numerical heat transfer and fluid mechanics*, McGraw-Hill, New York.
- Ulm, F.-J., Coussy, O., and Bažant, Z. P. (1999). "The "Chunnel" fire. I: Chemoplastic softening in rapidly heated concrete." *J. Eng. Mech.*, 125(3), 272–282.
- White, T. L., Foster, D., Jr., Wilson, C. T., and Schaich, C. R. (1995). "Phase II microwave concrete decontamination results," *ORNL Rep. No. DE-AC05-84OR21400*, Oak Ridge National Laboratory, Oak Ridge, Tenn.